2017

Study of Surface Passivation Behavior of Crystalline Silicon Solar Cells

Haider Ali
University of Central Florida

STUDY OF SURFACE PASSIVATION BEHAVIOR OF CRYSTALLINE SILICON SOLAR CELLS

by

HAIDER ALI
B.Tech, National Institute of Technology, Srinagar, India, 2009
M.E., Indian Institute of Science, Bangalore, India, 2011

A dissertation submitted in partial fulfilment of the requirements
for the degree of Doctor of Philosophy
in the Department of Materials Science and Engineering
in the College of Engineering and Computer Science
at University of Central Florida
Orlando, Florida

Spring Term
2017

Major Professor: Winston V. Schoenfeld

ABSTRACT

To achieve efficiencies approaching the theoretical limit of 29.4% for industrially manufactured solar cells based on crystalline silicon, it is essential to have very low surface recombination velocities at both the front and rear surfaces of the silicon substrate. Typically, the substrate surfaces feature contacted and uncontacted regions, and recombination should be limited for both to maximize the energy conversion efficiency.

Uncontacted silicon surfaces are often passivated by the deposition of silicon nitride (SiN_x) or an aluminum oxide film with SiN_x as capping layer (Al_2O_3/SiN_x stack). Further, proper surface preparation and cleaning of Si wafers prior to deposition also plays an important role in minimizing surface recombination. In the present work, the effect of various cleans based on different combinations of HCl, HF, HNO_3, and ozonated deionized water (DIO_3) on surface passivation quality of boron-diffused and undiffused {100} n-type Cz Si wafers was studied. It was observed that for SiN_x passivated Si, carrier lifetime was strongly influenced by cleaning variations and that a DIO_3-last treatment resulted in higher lifetimes. Moreover, DIO_3+HF+HCl→HF→DIO_3 and HNO_3→HF→HNO_3 cleans emerged as potential low-cost alternatives to HCl/HF clean in the photovoltaics industry.

Transmission electron microscopy (TEM) studies were carried out to get insight into the origin of variation in carrier lifetimes for different cleans. Changes in the surface cleans used were not found to have a significant impact on Al_2O_3/SiN_x passivation stacks.

However, an oxide-last cleaning step prior to deposition of SiN_x passivation layers was found to create a 1-2 nm SiO_x tunnel layer resulting in excellent carrier lifetimes.

For contacted regions, low surface recombination can be achieved using passivated carrier selective contacts, which not only passivate the silicon surface and improve the open circuit voltage, but are also carrier selective. This means they only allow the majority carrier to be transported to the metal contacts, limiting recombination by reducing the number of minority carriers. Typically, carrier selectivity is achieved using a thin metal oxide layer, such as titanium oxide (TiO_2) for electron-selective contacts and molybdenum oxide (MoO_x) for hole-selective contacts. This is normally coupled with a very thin passivation layer (e.g., a-Si:H, SiO_x) between the silicon wafer and the contact.

In the present work, TiO_2-based electron-selective passivated rear contacts were investigated for *n*-type c-Si solar cells. A low efficiency of 9.8% was obtained for cells featuring a-Si:H/TiO_2 rear contact, which can be attributed to rapid degradation of surface passivation of a-Si:H upon FGA at 350°C due to hydrogen evolution leading to generation of defect states which increases recombination and hence a much lower V_{oc} of 365 mV is obtained. On the other hand, 21.6% efficiency for cells featuring SiO_2/TiO_2 rear contact is due to excellent passivation of SiO_2/TiO_2 stack upon FGA anneal, which can be attributed to the presence of 1-2 nm SiO_2 layer whose passivation performance improves upon FGA at 350°C whereas presence of large number of oxygen vacancies in TiO_{2-x} reduces rear contact resistivity.

Likewise, MoO_x-based contacts were investigated as hole-selective front contacts for an *n*-type cell with a boron-doped emitter. It has been previously reported that cell efficiencies up to 22.5% have been achieved with silicon heterojunction solar cells featuring a front contact wherein MoO_x is inserted between a-Si:H(*i*) and hydrogenated indium oxide (IO:H). However, device performance and FF degrades upon annealing beyond 130°C. In this work, contact resistivity measurements by TLM technique in combination with TEM studies revealed that degradation of device performance is due to oxygen diffusion into MoO_x upon annealing in air which reduces concentration of oxygen vacancies in MoO_x and increases contact resistivity. The increase in contact resistivity reduces FF resulting in deterioration of device performance.

Dedicated to my family

ACKNOWLEDGMENTS

First and foremost, I would like to thank my PhD advisor Dr. Winston Schoenfeld whose professional guidance and scientific inputs made this work possible. I would also like to thank Dr. Kristopher Davis for mentoring me during my PhD dissertation and all the useful technical discussions I had with him.

I would like to thank Dr. Kevin Coffey, Dr. Jayan Thomas, Dr. Romain Gaume and Dr. Debashish Chanda for serving on my dissertation committee.

I would like to thank Dr. Helge Heinrich, Dr. Aniruddha Dutta and Matt Schneider for introducing me to the exciting world of transmission electron microscopy (TEM) and for helping me with the instrument training.

I would like to thank Dr. Sebastian Mack (Fraunhofer ISE, Germany), Dr. Xinbo Yang (formerly at Australian National University, Canberra) and Dr. James Bullock (UC Berkeley) for their contributions to this work.

I would like to thank the Material Characterization Facility (MCF) at UCF and its entire staff for their invaluable support.

I would like to thank Dr. Pat Looney and Dr. Feng Wang at Brookhaven National Laboratory (BNL) for providing me an opportunity to work there and for all their scientific and technical inputs.

I would like to acknowledge the financial support for this work by the U.S. Department of Energy, Office of Energy Efficiency and Renewable Energy, in the Solar Energy Technologies Program, under Award No. DE-EE0004947. I would also like to thank Qorvo, Apopka, FL for funding my PhD.

I would also like to thank administrative staff at MSE department at UCF and FSEC for all their support.

I would like to thank all my friends and lab mates for making my stay at UCF and Orlando a memorable one. A special thanks to my friends Ashish, Abhishek, Ankur and Sarfaraz for everything they have done for me.

Last, but not the least, I would like to thank my family for their encouragement and unwavering support throughout my academic career.

TABLE OF CONTENT

LIST OF FIGURES

LIST OF TABLES

CHAPTER 1:
INTRODUCTION

1.1 History of photovoltaics

In 1839, French physicist Edmond Becquerel observed that an electric voltage developed between two electrodes of an electrolytic cell when he shone light onto this system. This effect is known as the photovoltaic effect. Subsequently, attempts were made to develop devices that could convert light into electricity. These devices were known as photovoltaic solar cells. The first functional PV device based on Se wafers was developed by an American inventor named Fritts in 1883.[1-4]

The first commercial solar cell which was a p-n junction solar cell was developed in 1954 at Bell Laboratory by David Chapin, Calvin Fuller and Gerald Pearson. It was the first solar cell capable of converting enough of the sun's energy into power to run every day electrical equipment. Its efficiency was reported to be 6% and was used to power telephone lines in rural areas.[2, 5-7] In the same year, 6% efficient thin-film heterojunction solar cell based on Cu_2S/CdS was reported. A year later, RCA Lab, USA reported a 6% efficient GaAs p-n junction solar cell. Around the same period, similar efficiencies were also reported for CdTe thin films solar cells. A few years later in 1970, Alferov et al Ioffe Institute in USSR reported first heterojunction solar cell based on GaAlAs/GaAs.[4]

The year of 1973 is often regarded as the beginning of modern era of photovoltaics. In that year, group of PV researchers and representatives of various US government

scientific organizations met in the town of Cherry Hill, New Jersey, USA with the goal of evaluating the merits of PV and its potential applications. At the *Cherry Hill Conference*, decision was made to provide government support for research and development of PV which led to the formation of the US Energy Research and Development Agency which became the US Dept. of Energy. Later that year in October, major oil producing nations in the Persian Gulf led by Saudi Arabia imposed the first World Oil Embargo which led to quadrupling of international crude oil prices. This sent shock waves throughout the industrialized world and forced major world governments to initiate steps for reducing dependence on oil and instead focus more on alternate energy sources especially solar energy. It was only after the 1973 oil shock that major government policy decisions were taken in order to encourage research and application of photovoltaics in terrestrial applications.[4]

1.2 Need for solar energy

Today, most of the energy is generated by burning fossil fuels (coal, oil, natural gas) and other non-renewable sources. However, fossil fuel sources such as coal and natural gas are limited and there is pressing need to look for alternate sources of energy. Additionally, over dependence on fossil fuels for meeting energy requirements will increase greenhouse emissions at a time when there is a pressing need to address the problem of climate change. On the other hand, nuclear energy poses environmental problems related to storage or disposal of nuclear waste. Moreover, major nuclear accidents such as the one at Chernobyl in former Soviet Union on 26th April, 1986 and

more recently at Fukushima on 11th March, 2011 have exposed the looming dangers associated with nuclear technology. Moreover, with global estimated to be 7.3 billion people in 2015 and expected to grow to reach 8 billion by 2030, global energy demand is going to increase as well.[8] Moreover, as world economies develop, per capita energy consumption is going to increase as well. In such a situation, there is an ever-increasing need for mankind to explore alternate sources of energy which are clean and renewable.

Although wind, geothermal, hydroelectric and ocean thermal energy have emerged as promising alternative energy sources which are clean and environment friendly, they are limited by their low technical potential which is defined as the achievable energy generation of a technology, given system performance, topographic limitations, environmental, and land-use constraints.

On the other hand, solar energy is the earth's major renewable energy resource and the exploitation of the energy from the sun is the potential key to a sustainable energy production in future. Solar energy offers a very large amount of technical potential of over 1000 EJ which is nearly twice the 2010 global primary energy supply of 510 EJ.[9] Conversion of sunlight into electricity using photovoltaic cells emits essentially no toxic or greenhouse gases, it requires no moving parts and does not produce noise, while the material requirements are extremely low. Only production and disposal/recycling of devices are critical in their effects on the environment. Photovoltaic systems can be installed in principle in every region of the earth. With the energy from the sun being so

plentiful, the challenge then lies on scientists and engineers to harness this energy using efficient and cost-effective solar cells.

1.3 Physics of solar cells

Silicon is an indirect bandgap semiconductor with a band gap of 1.1 eV. By doping it with boron or phosphorous, it can be made p-type or n-type respectively. When p-type (B-doped) and n-type (P-doped) are brought together, a p-n junction is formed. A solar cell is a typical p-n junction semiconductor diode which can convert incident radiation into useful electrical work. When light is incident on the solar cell, the incoming photons are absorbed and their energy is converted into electron-hole pairs. Each of the photons with an energy $h\nu > E_{gap}$ (band gap) can give energy equal to E_{gap} to the photo-generated electron-hole pair while the excess energy ($h\nu - E_{gap}$) is lost due to thermalization. The photo-generated electron-hole pairs generated within the depletion region are then separated by the built-in voltage within the depletion region (Figure 1-1).

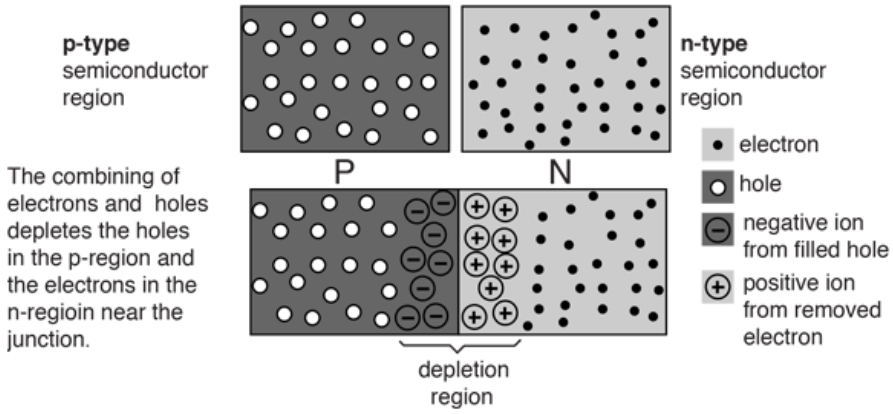

Figure 1-1: Schematic of depletion region for a p-n junction[10]

The majority carriers in p-type semiconductor are holes while electrons are the majority carriers in n-type semiconductors. The free electrons from n-type migrate over the p-n junction to recombine with holes in the p-type semiconductor. A region is created wherein all the electrons and holes are recombined. This region at the junction is termed the depletion zone. At the junction, a negative charge develops at the edge of the depletion zone in the p-type semiconductor while a net positive charge forms at the edge in the n-type semiconductor. Therefore, a potential develops within the material known as built-in voltage. This built-in voltage drives the photo-generated electrons through to the external circuit. The product of electric current and voltage is the electric power that can be used to run varied applications.

To understand the electronic behavior of a solar cell, it would useful to create an equivalent electrical model. An ideal solar cell can be thought of as a current source in parallel with a diode. To account for losses due to resistance at the contacts as well as due to shunting paths within the cell, series and shunt resistances are added to the equivalent circuit. The dark (non-illuminated) characteristics of the diode and the photogenerated current and the solar cell equivalent circuit are shown in Figure 1-2.

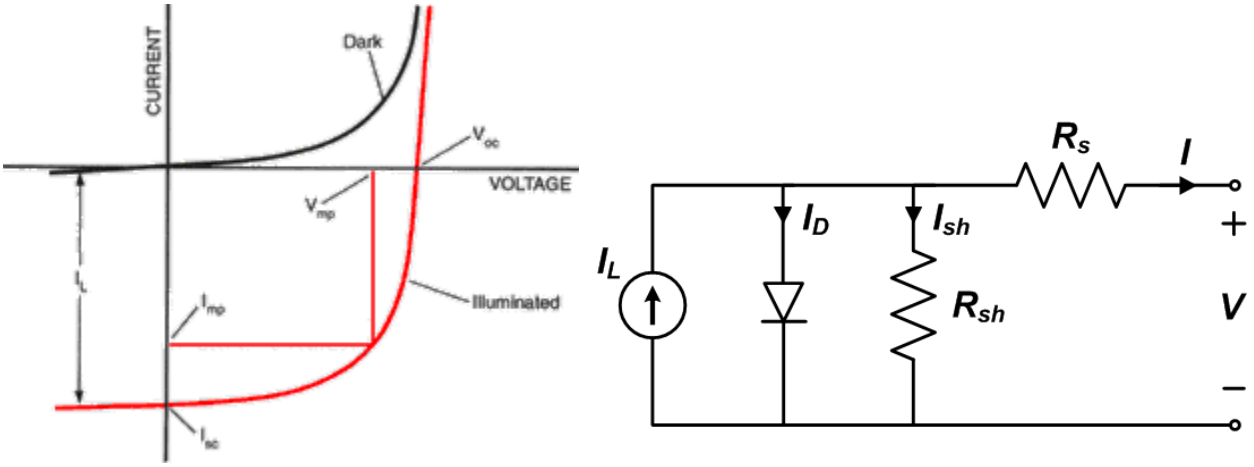

Figure 1-2: (a) I-V curve of a solar cell under dark and illuminated conditions.[11] (b) Equivalent circuit of a solar cell.[12]

The equation for an I-V curve of a solar cell follows from the equivalent circuit shown in Figure 1-2(b) and is given by the relation

$$I = I_L - I_D - I_{sh} \tag{1-1}$$

$I = output\ current$

$I_L = photogenerated\ current$

$I_D = diode\ current$

$I_{sh} = shunt\ current$

When diode characteristics and Kirchhoff's law are applied to equation 1-1, we get

$$I = I_L - I_0\left\{e^{\frac{q[V+IR_S]}{mkT}} - 1\right\} - \frac{V+IR_S}{R_p} \tag{1-2}$$

$I_0 = reverse\ saturation\ current$

$V = output\ voltage$

$R_p = shunt\ resistance$

$R_S = series\ resistance$

$m = diode\ ideality\ factor$

1.4 Device parameters

1.4.1 Short circuit current (I_{sc})

The short-circuit current is the current through the solar cell when the voltage across the solar cell is zero (i.e., when the solar cell is short circuited). It is purely due to the generation and collection of photo-generated carriers. Hence, for an ideal solar cell, I_{sc} equals the I_L. In other words, I_{sc} is the largest current which may be drawn from the solar cell.

I_{sc} can be increased by improving the light absorption within the cell. This can be accomplished using anti-reflection coatings (ARCs) at the front surface. Alternatively, surface texturing is also employed to increase the amount of light entering the cell by deflecting the incident light after reflection back to be incident on cell another time. Furthermore, surface texturing can also reduce losses due to reflection at the rear by

increasing the angle of incident at the front surface which results in light being reflected internally within the cell. These processes within a surface textured substrate are illustrated in Figure 1-3.

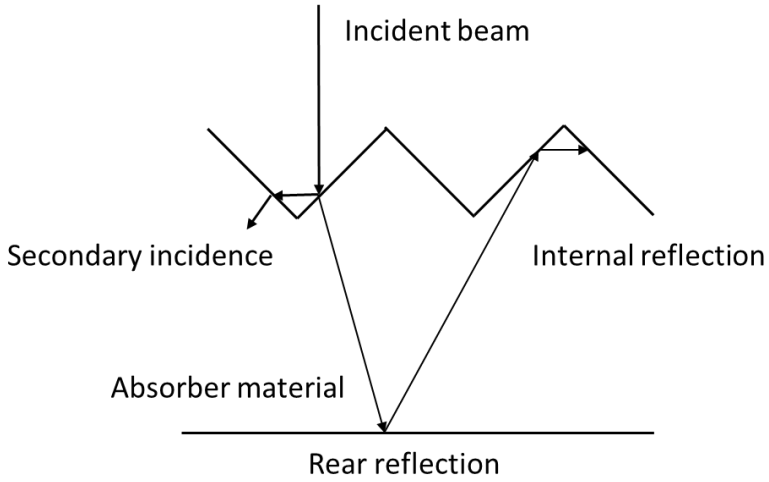

Figure 1-3: Schematic illustration of reducing surface reflectance and increased light-trapping by surface texturing

1.4.2 Open circuit voltage (V_{oc})

The open-circuit voltage is the maximum voltage available from a solar cell, and this occurs at zero current. The open-circuit voltage corresponds to the amount of forward bias on the solar cell due to the bias of the solar cell junction with the light-generated current. As evident from equation, V_{oc} is dependent on photo-generated current (I_L) and reverse saturation current (I_0). Since I_0 is caused by recombination within the cell, reducing the recombination reduces I_0 and increases V_{oc}. Recombination will be discussed in detail in chapter 2.

1.4.3 Fill factor (FF)

To obtain maximum power from cell, I_{sc} and V_{oc} needs to be maximized. However, no useful power can be obtained at these operating conditions. The point at which maximum power can be obtained from the cell is known as maximum power point (MPP). Ideally, this is where the solar cell should be operated.

Another important cell parameter is the fill factor(FF) which relates MPP to I_{sc} and V_{oc} and is given by the relation

$$FF = \frac{P_{max}}{V_{oc} I_{sc}} \tag{1-3}$$

$$P_{max} = V_M I_M \tag{1-4}$$

$V_M = voltage\ at\ maximum\ power$

$I_M = current\ at\ maximum\ power$

The FF of a cell is dependent on the series resistance R_s and shunt resistance R_{sh}. As evident from equation, power is dissipated across R_s as current flow though the cell. As a results FF and maximum power reduces with increase in R_s. The power loss due to R_s is given by the relation

$$P_{loss,R_s} = \left(1 - \frac{I_M R_s}{V_M}\right) \tag{1-5}$$

For small values of R_s, $I_M \approx I_{sc}$ and $V_M \approx V_{oc}$. Therefore, FF loss can be given by the relation

$$FF_{loss,R_s} \approx \left(1 - \frac{I_{sc}R_s}{V_{oc}}\right) \quad (1\text{-}6)$$

On the other hand, shunt resistance provides an alternate path for the dark current to flow and reduced cell output. For an ideal cell, $R_{sh} \approx \infty$. However,if value of Rsh is substanially lower, FF and power loss is given by the relation

$$FF_{loss,R_{sh}} \approx P_{loss,R_{sh}} \approx \left(1 - \frac{V_{oc}}{I_{sc}R_{sh}}\right) \quad (1\text{-}7)$$

1.4.4 Conversion efficiency (η)

It is the percentage of the solar energy shining on a solar cell that is converted into usable electricity. Improving this conversion efficiency is a key goal of research and helps make PV technologies cost-competitive with conventional sources of energy. It is defined by the relation

$$\eta = \frac{V_{oc}I_{sc}FF}{P_{in}} \quad (1\text{-}8)$$

$$P_{in} = incident\ power\ taken\ as \frac{1kW}{m^2}\ corresponding\ to\ AM\ 1.5G\ solar\ spectrum$$

Typically, terrestrial solar cell efficiencies are reported under illumination from AM 1.5G spectrum which has an integrated power density of 1kW/m^2. Here AM represents Air Mass which is a measure of how absorption in the atmosphere affects the spectral content and intensity of the solar radiation reaching the Earth's surface. It is defined by the relation

$$AM = \sqrt{1 + \left(\frac{S}{H}\right)^2} \quad (1\text{-}9)$$

$S = length\ of\ a\ shadow\ cast\ by\ an\ object\ of\ height\ H$

Just above the Earth's atmosphere, the radiation intensity, or Solar Constant, is about 1.353 kW/m^2 and the spectral distribution is referred to as an air mass zero (AM0) radiation spectrum. The AM1.5G spectrum is representative of the spectral irradiance that reaches the earth's surface at a solar zenith angle of 48.2°. It is intended to take into account various atmospheric effects such as absorption and scattering that takes places due to presence of water vapor and other elements.

1.5 Silicon PV

Ever since the first commercial solar cell based on c-Si was reported by Bell Laboratories in 1954, c-Si has dominated the PV industry and this trend is likely to continue in the foreseeable future.

Currently, nearly 90% of PV modules manufactured today are based on c-Si wafers which includes both mono- and multi-crystalline Si. A major driving force behind this is the fact that wafer-based silicon has been widely used in the integrated circuit industry for so long, which enables us to utilize a technology that is already well understood for manufacturing PV cells and modules. Other advantages of c-Si include high module efficiency (16 – 22%), low manufacturing cost (\$/W_p), excellent long-term module stability (> 20 years), material abundance and non-toxicity.[4, 13]

Although, most of the industrially manufactured solar cells have achieved energy conversion efficiencies of 17-21%, it is still lower than at the laboratory scale efficiencies of up to 26.3% and 21.3% that have been achieved for mono-crystalline and multi-crystalline silicon solar cells respectively and even further lower than theoretical upper limit of efficiency as prescribed by Shockley-Quisser limit of 29%. [14, 15]

The lower efficiencies obtained for industrially manufactured solar cells is mainly due to electronic recombination occurring at the surfaces resulting in lower V_{oc}. Hence, a reduction in surface recombination is essential to obtain high efficiency industrial solar cells. This is possible by employing effective surface passivation mechanism in these cells.[14, 16] Therefore, a lot of research has been done recently on various passivation layers and passivated contacts.

In this work, various aspects of surface passivation of c-Si solar cells were investigated with the help of transmission electron microscopy (TEM) to understand the passivation performance of SiN_x and Al_2O_3/SiN_x passivated Si as well as that of carrier-selective contacts namely TiO_2 (electron-selective) and MoO_x (hole-selective). An overview of surface passivation and electron microscopy will be presented in chapters 2 and 3 respectively. The impact of surface preparation on passivation performance of SiN_x and Al_2O_3 will be discussed in chapters 4 and 5. The role of electron-selective TiO_2-based rear contacts and hole-selective MoO_x-based front contacts on device performance will be discussed in chapters 6 and 7 respectively.

CHAPTER 2:
SURFACE PASSIVATION

2.1 Carrier recombination

When an electron in the valence band (VB) absorbs a photon ($hv>E_g$) and undergoes a transition to the conduction band (CB) then we have an extra electron in CB and a hole in VB. This process by which an electron-hole pairs are created is known as generation. When light falls on the solar cell, electron-hole pairs are generated which are responsible for conversion of light energy into electrical energy. However, if the electrons and holes recombine in the bulk or at the surface of the solar cell before they can reach external circuit, then it is known as recombination. Recombination reduces the number of available charge carriers and thereby reducing the cell output.

The equilibrium concentration of electrons and holes is given by the equation

$$n_0 p_0 = n_i^2 \qquad (2\text{-}1)$$

$n_0 = equilibrium\ concentration\ of\ electrons$

$p_0 = equilibrium\ concentration\ of\ holes$

$n_i = intrinsic\ carrier\ concentration$

When excess electrons and holes are generated, we have

$$n = n_0 + \Delta n \qquad (2\text{-}2(a))$$

$$p = p_0 + \Delta p \qquad (2\text{-}2(b))$$

$n = concentration\ of\ electrons$

$p = concentration\ of\ holes$

$\Delta n = excess\ electrons$

$\Delta p = excess\ hole$

These excess carriers exist as such in silicon for some time carrying current and generating voltage in the solar cell. If there are no trapping effects and no band bending, we have $\Delta n = \Delta p$. Then the average time taken by an electron-hole pair to recombine is given by

$$\tau = \frac{\Delta n}{U} \qquad (2\text{-}3)$$

$\tau = recombination\ lifetime$

$U = rate\ of\ recombination$

Therefore, higher efficiencies can be achieved in solar cells by increasing the recombination lifetime which is analogous to reduction of recombination rate. For this purpose, it is important to understand the recombination mechanisms that are taking place in a solar cell.

2.2 Recombination mechanisms

In any solar cell, both at the surface as well as in the bulk, there are mainly three recombination mechanisms that are taking place namely:

- Radiative recombination
- Auger recombination
- Shockley-Read-Hall recombination

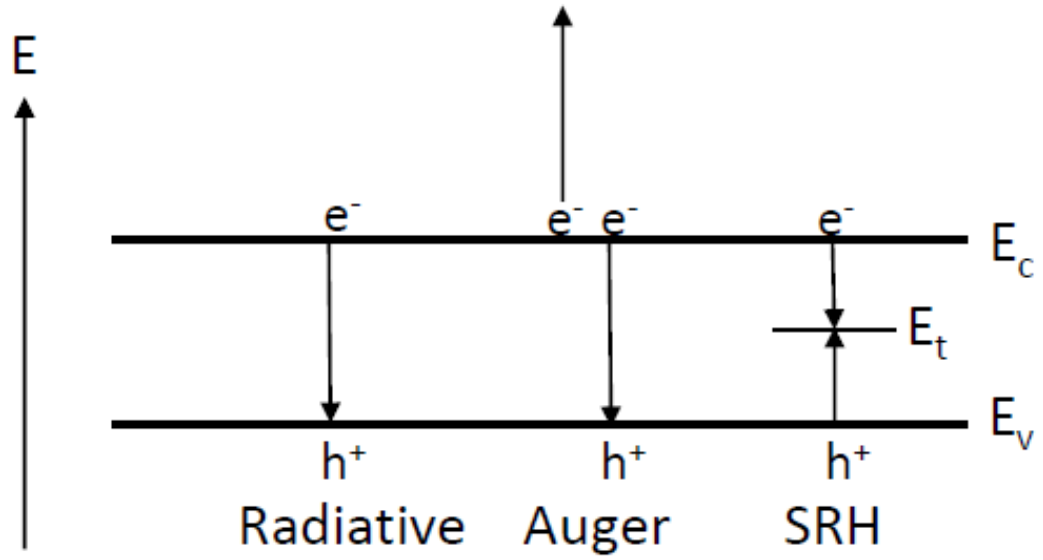

Figure 2-1: Schematic of recombination mechanism

2.2.1 Radiative recombination

In this mechanism, an electron from a conduction band recombines with a hole in the valence band and excess energy is released as a photon. The rate of radiative recombination is given by

$$U_{rad} = B(np - n_i^2) \quad (2\text{-}4)$$

$U_{rad} = rate\ of\ radiative\ recombination$

$B = coefficient\ of\ radiative\ recombination$

This mechanism, however, is significant only in direct band gap semiconductors. It is negligible in case of indirect band gap semiconductors such as silicon.

2.2.2 Auger recombination

Auger recombination, also known as band-to band recombination, involves three carriers. In this process, when an electron and a hole recombine, the excess energy is given to a third carrier which can be either an electron in conduction band or a hole in the valence band. This mechanism is particularly important at high doping concentration in case of silicon. The rate of Auger recombination is given by

$$U_{rad} = \left(C_n n + C_p p\right)(np - n_i^2) \quad (2\text{-}5)$$

$U_{rad} = rate\ of\ Auger\ recombination$

$C_n = electron\ Auger\ coefficient$

$C_p = hole\ Auger\ coefficient$

2.2.3 Shockley Read Hall recombination

This mechanism involves defects. These defects can be impurities, dislocations or other imperfections in the crystal lattice because of which an allowed energy state exists in the forbidden region of silicon. These energy states within the forbidden region can trap an electron/hole. If a hole/electron having sufficient energy can reach there and stay for sufficient time, then recombination occurs. The rate of SRH recombination is given by

$$U_{SRH} = \frac{np - n_i^2}{\tau_{p_0}(n + n_i\, exp\left(\frac{E_t - E_i}{KT}\right)) + \tau_{n_0}(p + n_i\, exp\left(\frac{E_i - E_t}{KT}\right))} \quad (2\text{-}6)$$

$$\tau_{p_0} = \frac{1}{\sigma_p v_{th} N_t}$$

$$\tau_{n_0} = \frac{1}{\sigma_n v_{th} N_t}$$

$\tau_{p_0} = hole\ capture\ time\ constant$

$\tau_{n_0} = electron\ capture\ time\ constant$

$E_t = energy\ level\ of\ trap$

$E_i = intrinsic\ energy\ level$

$\sigma_p = hole\ capture\ cross - section$

$\sigma_n = electron\ capture\ cross - section$

$N_t = density\ of\ defects$

2.3 Surface recombination

Surface recombination describes the recombination that takes place at the surface of the semiconductor. In case of silicon, it is mainly due to presence of large number of silicon dangling bonds at the surface. The contribution of radiative and Auger recombination at the silicon surface is not significant. The net recombination at the surface is given by the relation

$$U_s = S\Delta n_s \tag{2-7}$$

$U_s = rate\ of\ recombination\ at\ surface$

$S = surface\ recombination\ velocity$

$\Delta n_s = excess\ carrier\ concentration\ at\ surface$

2.4 Effective lifetime

The effective carrier lifetime is given by

$$\frac{1}{\tau_{eff}} = \frac{1}{\tau_{rad}} + \frac{1}{\tau_{Auger}} + \frac{1}{\tau_{SRH}} + \frac{1}{\tau_S} \tag{2-8}$$

$\tau_{eff} = effective\ carrier\ lifetime$

$\tau_{rad} = carrier\ lifetime\ due\ to\ radiative\ recombination$

$\tau_{Auger} = carrier\ lifetime\ due\ to\ band - to - band\ i.e.\ Auger\ recombination$

$\tau_{SRH} = carrier\ lifetime\ due\ to\ defects\ i.e.\ SRH\ recombination$

$\tau_S = carrier\ lifetime\ due\ to\ surface\ recombination$

When light falls on a solar cell, generation of electron-hole pairs takes place. However, many of these electrons and holes recombine before reaching the external circuit and no useful electrical work is done. To minimize these losses, τ_{eff} must be high enough so that carriers (namely electrons and holes) have sufficient time to reach the external circuit before they recombine. To achieve this, both bulk as well as surface recombination needs to be minimized. Bulk recombination can be reduced by using better quality material which is free of crystallographic defects, impurities and other imperfections. To reduce surface recombination, a good surface passivation is required which is discussed in next section.

2.5 Surface passivation

The rate of surface recombination expressed as a function of interface defect density, electron and hole capture cross sections, electron and hole densities is given by

$$U_s = \frac{(n_s p_s - n_i^2) v_{th} N_{it}}{\frac{n_s + n_1}{\sigma_p} + \frac{p_s + p_1}{\sigma_n}} \qquad (2\text{-}9)$$

$N_{it} = interface\ defect\ density$

n_1 & p_1 $= statistical\ factors$

σ_n&$\sigma_p = electron\ and\ hole\ capture\ cross-sections$

If we assume that $n_1, p_1, n_i \ll n_s, p_s$ and define $S_{n/p} = \sigma_{n/p} v_{th} N_{it}$, then we have

$$U_s \approx \frac{n_s p_s}{\frac{n_s}{s_p} + \frac{p_s}{s_n}} \quad (2\text{-}10)$$

However, the above equation is valid only under the assumption that there is a single energy level associated with surface defects are located at midgap. However, the energy levels associated with surface defects are distributed throughout the band gap.

From the above equations, it is evident that the rate of surface recombination is directly proportional to the term $n_s p_s - n_i^2$. This term represents the deviation of carrier concentration away from equilibrium values because of illumination.

To reduce surface recombination, the surface needs to be passivated. This can be done by:

- Chemical passivation: it involves a reduction in N_{it} by deposition of a suitable passivation layer on wafer surface.

- Field effect passivation: it involves reduction in density of one type of carrier (either electron or hole) by suitably doping the back and front wafer surfaces to from back and front surface fields or by use of suitable dielectric film that possess stable fixed charges.

All surface passivation techniques employ either one or both surface passivation mechanisms. One of these techniques is the use of dielectric films as a passivation layer. These dielectric films are described in detail in the next section.

2.6 Dielectric films

The dielectric films used for surface passivation in c-Si solar cells employs both surface passivation mechanisms. The dielectric films which are of importance for surface passivation in c-Si solar cells include SiO_2, a-SiN_x:H, a-Si:H, Al_2O_3, HfO_2.

2.6.1 Silicon oxide (SiO_2)

Thermally grown SiO_2 is an important passivation material for c-Si because of its ability to provide low surface recombination velocities. Very low S_{eff} values (< 10 cm/s) has been observed for SiO_2 after forming gas anneal. Hydrogen is introduced during anneal which can passivate the dangling bonds in Si leading to very low defect densities and consequently, an excellent chemical passivation. On the other hand, field-effect passivation is not significant in SiO_2 because of relatively low values of fixed charge. Despite the advantages, higher temperatures and longer oxidation required for SiO_2 has restricted its widespread usage for c-Si solar cells.[14, 17, 18]

2.6.2 Hydrogenated amorphous silicon nitride (a-SiN_x:H)

a-SiN_x:H is the most widely used dielectric in c-Si solar cells. It has the added advantage of having optimal refractive index, hence it acts as an anti-reflection coating as well. The presence of large amount of Hydrogen (10-15 at %) helps in bulk passivation of multicrystalline silicon and increases bulk lifetime. Passivation mechanism of a-SiN_x:H is strongly dependent on N content. For low N content, only chemical passivation is significant. At higher N content, significant amount of field effect passivation is observed. Being a positively charged dielectric, it is well suited for passivation of n-type surfaces. But for p-type surface, it can cause shunting effect leading to current losses in the solar cell. [14, 19, 20]

2.6.3 Hydrogenated amorphous silicon (a-Si:H)

Hydrogenated amorphous silicon films deposited by PECVD have been shown to possess S_{eff} as low as 2 cm/s. The passivation behavior in these films is mainly due to chemical passivation. These films can passivate both diffused as well as undiffused p-type and n-type surfaces. Doped a-Si:H have been used in HIT (heterojunction with intrinsic thin layer) cells in which efficiencies up to 23.7% and high V_{oc} (>700 mV) have been achieved. However, these films have significant absorption in visible part of the solar spectrum resulting in parasitic absorption. Moreover, these films lack thermal stability at higher temperatures.[14, 21, 22]

2.6.4 Aluminum oxide (Al_2O_3)

Aluminum oxide deposited by plasma assisted ALD have been shown to provide excellent surface passivation to both undiffused as well as highly doped p-type surfaces as well as lightly doped n-type surface. The surface passivation of Al_2O_3 is due to relatively low interface defect density ($D_{it}<10^{11}/cm^2.eV$) resulting in good chemical passivation and a high value of negative fixed charge density ($Q_f = 10^{12} – 10^{13}/cm^2$) that leads to excellent field effect passivation. Surface recombination velocities as low as 5 cm/s have been obtained with Al_2O_3 upon annealing. For solar cells that use Al_2O_3 as passivation layer, cell efficiencies up to 21.5% have been achieved in Passivated emitter and rear cell (PERC) and up to 23.9% in passivated emitter and rear locally diffused (PERL) cells. [14, 23-26]

2.6.5 Hafnium oxide (HfO_2)

Recently, HfO_2 has been investigated as a potential candidate for surface passivation because of its negligible absorption in visible region of the solar spectrum, good electrical interface properties and high thermal stability. Surface recombination velocity in the range of 73 cm/s have been obtained for both p-type and n-type c-Si surfaces which have ALD deposited HfO_2 as passivation layer.[27, 28]

2.7 Carrier selective contacts

Another technique that has been employed to reduce surface recombination in c-Si solar cells is use of Carrier selective contacts (CSCs). CSCs not only passivate the silicon surface but are also carrier-selective in nature i.e. they only allow either electrons or holes to pass through. The incorporation of CSCs into silicon solar cell improves cell efficiency by providing excellent surface passivation at contacted regions resulting in a high open-circuit voltage V_{oc}, and simplified current flow pattern resulting in a high fill factor FF.

Typically, a CSC can be achieved by deposition of conducting layer over an ultra-thin passivation layer. For instance, a stack of ultra-thin SiO_2 and doped hydrogenated amorphous silicon (a-Si:H) can act as an electron-selective or a hole-blocking layer. Although higher efficiencies have been achieved for solar cells with CSCs based on a-Si:H and SiO_2, they suffer from certain drawbacks that include thermal instability and parasitic photon absorption of a-Si:H films, complicated deposition process, and high fabrication cost. Moreover, the doped a-Si:H layers are deposited by plasma-enhanced chemical vapor deposition (PECVD), which is a capital-intensive system with mandatory safety systems because of the pyrophoric silane and toxic boron/phosphorous gas precursors employed. Therefore, it is essential to develop high quality CSCs that can be deposited easily, economically, and safely with minimal hazardous risks.[29]

Transition metal oxides have emerged as promising candidates for use as CSCs in c-Si solar cells. Typically, these CSC contain an ultra-thin layer of metal oxide which act as electron-blocking or hole-blocking layer.

For instance, sub-stoichiometric metal oxides such as tungsten oxide (WO_x), vanadium oxide(VO_x) and molybdenum oxide (MoO_x) can act as electron-blocking layer to silicon absorber because of their wide band gap and high work function resulting in a large conduction band offset. [30-33]

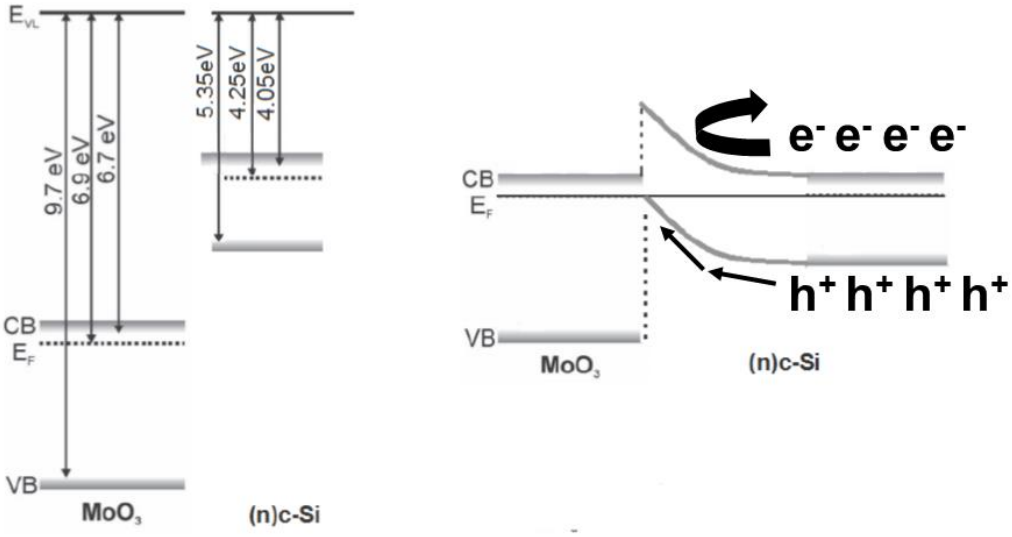

Figure 2-2: MoO_3-Si band diagram when isolated (left) and after forming a junction (right)[34]

Likewise, TiO_2 can act as hole-blocking layer due to a small conduction band offset ($\Delta E_c \approx 0.05$ eV), which allows electrons to pass through the TiO2 layer and a large valence-band offset ($\Delta E_v \approx 2.0$ eV), which results in holes being blocked.[29, 35]

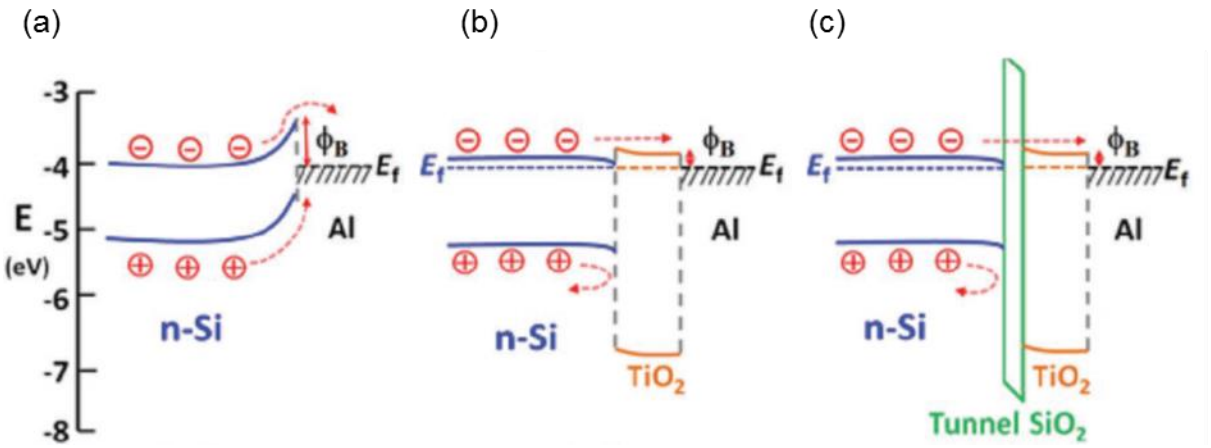

Figure 2-3: Bandgap alignments of the n-type silicon solar cells with different rear contacts (a) n-Si/Al, (b) n-Si/TiO_2/Al, (c) n-Si/SiO_2/TiO_2/Al[29]

CHAPTER 3:
ELECTRON MICROSCOPY

3.1 Introduction

Electron microscopy is one of the most powerful tools for micro- and nano-structural characterization of materials that employs a beam of high-energy electrons to examine objects. It can reveal valuable information about the topography, morphology, crystallography and chemical composition.

An electron microscope(EM) employs a beam of high energy electrons is used to form an image of the specimen. The advantage of EMs over optical microscopes is that it allows us to obtain much higher magnifications to the order 2Mx which is several orders of magnitude higher than that obtained by optical microscopes. In both electron and light microscopes resolution is limited by wavelength. The greater resolution and magnification of the electron microscope is due to the wavelength of an electron, its de Broglie wavelength, being much smaller than that of a light photon, electromagnetic radiation. However, EMs are large, expensive pieces of equipment, generally standing alone in small, specially designed room and trained personnel are required to operate them.

In EM, beam of electrons under a high acceleration voltage (≈ 10-300 KV) are used. In contrast to glass lenses used in optical microscope, electromagnetic lenses are used in electron microscopes (EM). The de Broglie wavelength of the electrons is dependent on the acceleration voltage and is given by

$$\lambda_{rel} = \frac{h}{\sqrt{2em_0U(1+\frac{eU}{2m_0c^2})}} \quad (3\text{-}1)$$

$\lambda_{rel.} = relativistic\ de\ Broglie\ wavelength\ of\ electrons$

$h = Planck's\ constant$

$e = charge\ of\ electron$

$m_0 = rest\ mass\ of\ electron$

$U = acceleration\ voltage$

$c = speed\ of\ light$

Higher the acceleration voltage, smaller will be de Broglie wavelength of electrons. Since, smaller wavelengths lead to a higher resolution, therefore increasing the acceleration voltage increases the resolution of the EM. For instance, at 10KV, de Broglie wavelength of electron is ≈ 0.12 Å which is ≈10^4 smaller than of visible light. Thus, it is possible to obtain a very high resolution in EM which is several orders of magnitude higher than that of an optical microscope.

3.2 Scanning electron microscopy

When a beam of high energy electrons is focused on the specimen, these electrons interact with the sample and several signals are generated from electron-

sample interactions, which can reveal useful information about surface morphology, chemical composition, and texture and crystal structure.

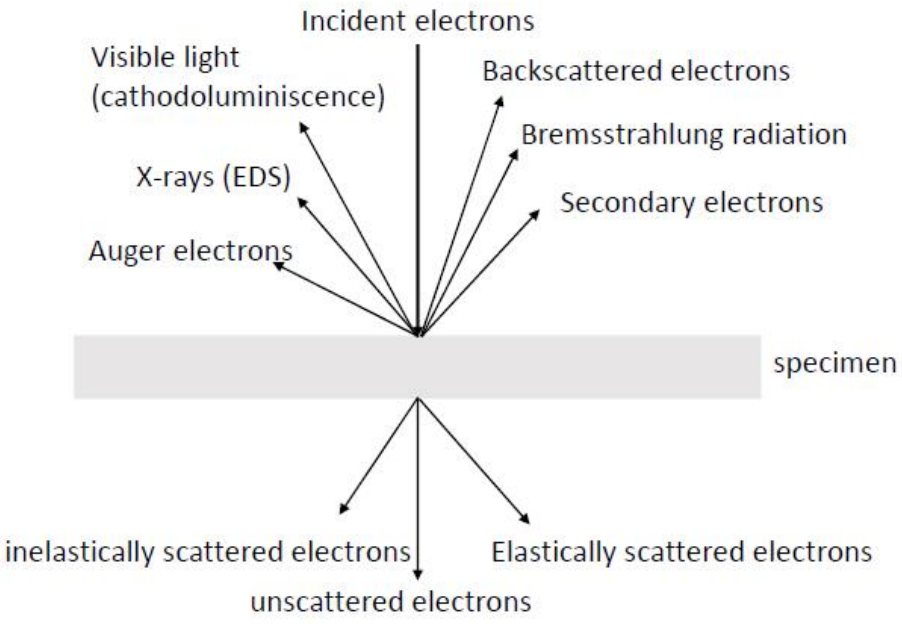

Figure 3-1: electron-matter interaction

In scanning electron microscope, a focused beam of high energy electrons is used to scan the sample surface. The electron-sample interactions generate secondary electrons (SE), backscattered electrons (BSE) and characteristic x-rays which are detected by various detectors. Secondary electrons are used to form SE image which gives us information about surface morphology. Backscattered electrons are used to form a BSE image in which contrast is due to atomic weight wherein the regions having lower atomic weight phases appear dark. Characteristic x-rays are detected by energy dispersive x-ray spectroscopy (EDS) detectors which gives us information about chemical composition.

Typically, a resolution of ≈ 1-20 nm can be obtained in an SEM which is several orders of magnitude than that of an optical microscope. However, it is still at least an order of magnitude than what can be achieved in transmission electron microscope (TEM). On the other hand, a TEM is much more expensive than an SEM and requires lot more skills to operate it.

3.3 Transmission Electron Microscopy

A Transmission Electron Microscope (TEM) consists of an electron gun that acts an electron source; a system of condenser lenses for reducing the area illuminated by electron beam; an objective lens, an imaging system consisting of diffraction lens, intermediate and projector lenses; and a viewing screen. A high-energy electron beam (≈ 100-300 KV) is focused onto a very thin specimen (≈ 20-100 nm) of interest. The electrons interact with specimen and the transmitted electrons form the image which can be projected on a viewing screen.

Because of very high accelerating voltage of electrons, their de Broglie wavelength is very small (≈ 0.02Å). If lens aberrations and other corrections are considered, resolution of ≈ 2Å can be obtained, which is of the order of the size of an atom. Therefore, images having atomic resolution can be obtained with the help of TEM.

There are two basic operations of the TEM imaging system: diffraction mode, image mode. In the diffraction mode, the diffraction pattern is projected onto the viewing screen. The intermediate lens selects the back focal plane of the objective lens as its

object. In image mode, the image is projected onto the screen. In each case the intermediate lens selects the image plane of the objective lens as its object.

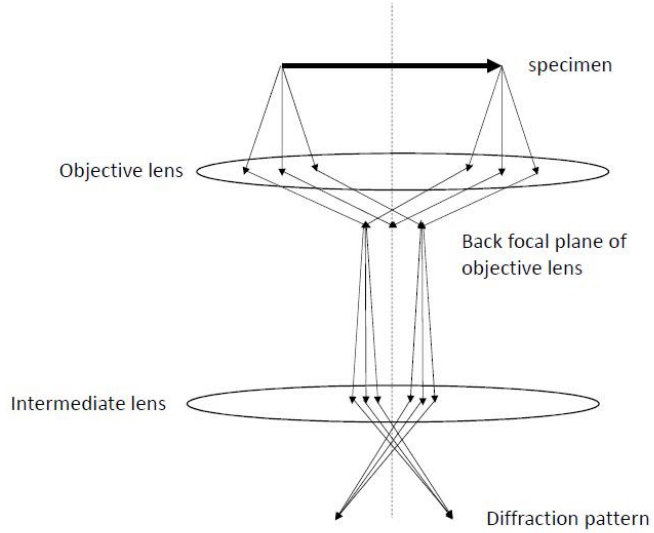

Figure 3-2: diffraction mode

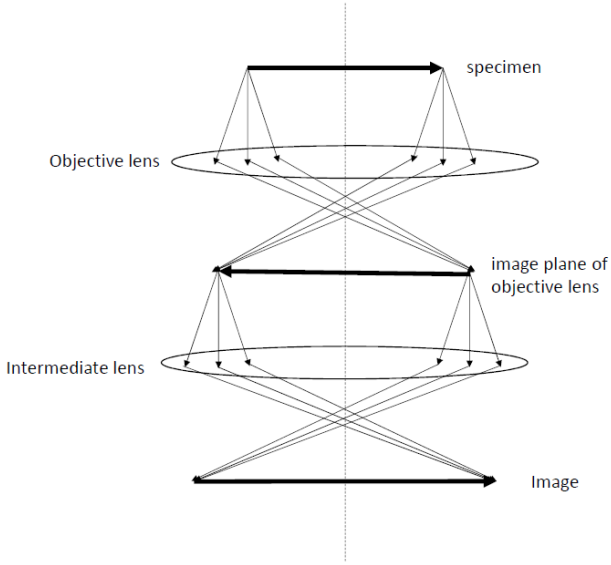

Figure 3-3: image mode

3.4 Conventional Transmission Electron Microscopy (CTEM)

The conventional TEM mode uses a broad, nearly parallel electron beam with a diameter of several micrometers. Apertures in the back focal plane and in the image plane may be applied to increase the contrast or to select an area of interest.

3.4.1 Bright-field and dark-field TEM

If the objective aperture is centered about the undiffracted beam, then only the undiffracted beam (or few of the low-indexed Bragg reflections) will contribute to first image formation in image plane of objective lens. This is known as bright-field conditions (Fig. 3-4 (a)). This result in an enhanced contrast in the micrograph compared to image without aperture.

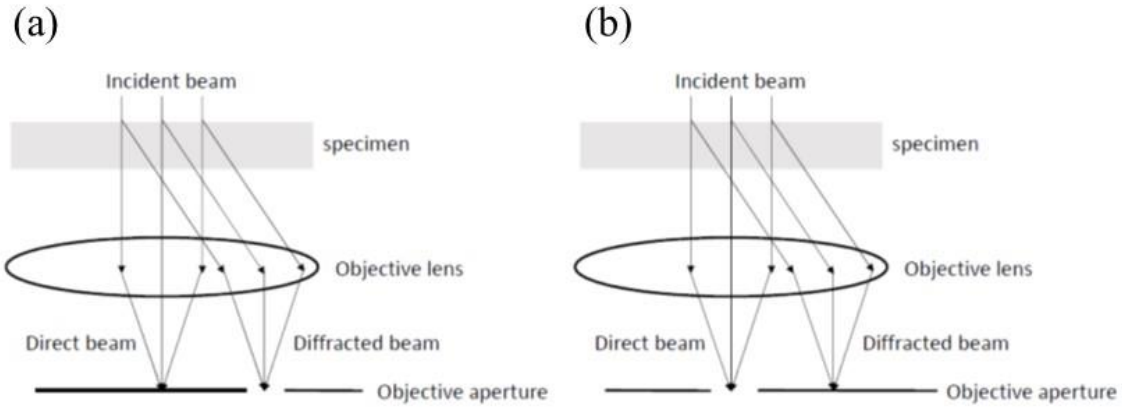

Figure 3-4: Bright field and dark field imaging

On the other hand, if a specific diffracted beam is used for first image formation then it is dark-field conditions. As shown in (Fig.3-4(b)), the aperture is displaced to select scattered electrons that travel off the optic axis. However, the problem with this kind of imaging is that the more off-axis the electrons are the greater the aberrations and astigmatism they suffer which makes it difficult to focus the image. In dark-field imaging mode only those regions appear bright which contribute to the Bragg reflection in the objective aperture. All other regions appear dark

3.4.2 Selected-area diffraction (SAD)

As shown in Fig.3-5, the diffraction pattern contains electron from the whole area of specimen illuminated by the electron beam. Such a pattern is not very useful because the specimen is often buckled. Moreover, if the direct beam is very intense it may damage the viewing screen. Therefore, to select a specific area of specimen to contribute to diffraction pattern and to reduce the intensity of direct beam on the viewing screen, selected-area diffraction (SAD) technique is used. In this technique, an aperture is inserted in image plane of objective lens centered on the optical axis that creates a virtual aperture at the plane of the specimen as shown in Fig.3-5.

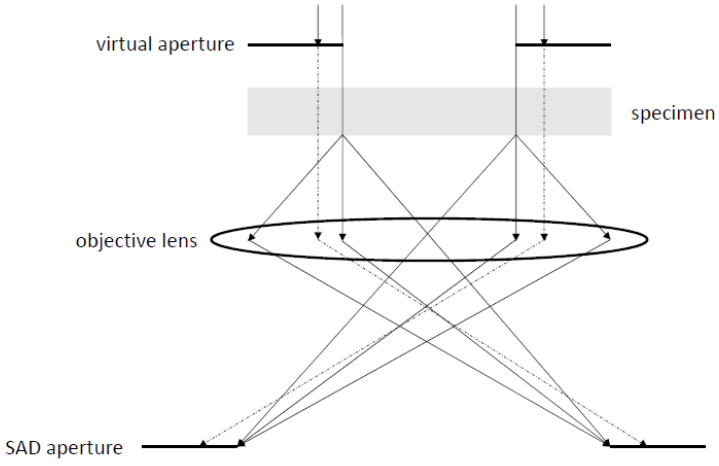

Figure 3-5: selected area diffraction (SAD)

3.5 Scanning transmission electron microscopy (STEM)

In STEM mode, a highly convergent electron probe having a diameter of few angstroms is used to scan the sample with the help of deflection coils. Electrons that impinge on the specimen generate X-rays or they lose energy upon interaction with electrons within specimen. These processes can be used for chemical analysis of any specific area of specimen. Moreover, diffracted electrons can be detected by an annular detector to form an image of the specimen.

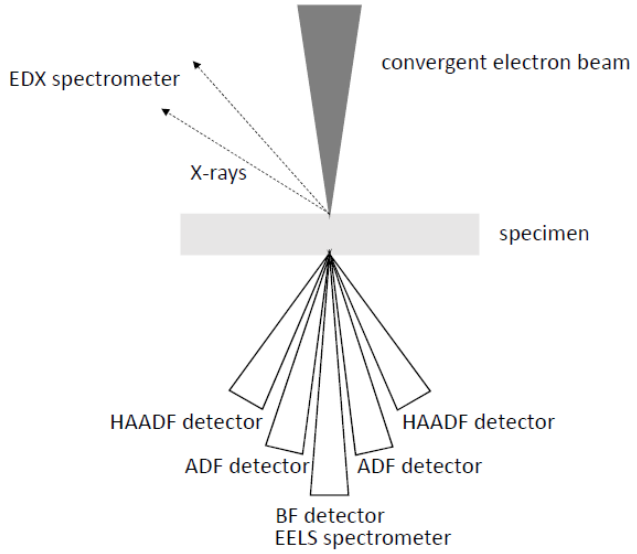

Figure 3-6: schematic of STEM mode

3.5.1. High-angle annular dark field (HAADF)

As shown in Fig.3-6, a high-angle annular dark field (HAADF) detector is used for high-angle collection of electrons (>50mrad to avoid Bragg effects). At shorter camera lengths, the collection angle increases and hence only elastically scattered electrons are detected. Thus, a HAADF-STEM image with a high Z-contrast can be obtained where the lower Z region appears dark.

3.5.2 Energy Dispersive X-ray spectroscopy (EDS)

As electrons from the electron probe interact with inner-shell electrons present within the specimen; the latter are ejected as secondary electrons leaving behind empty lower energy states. Electrons from higher energy states subsequently occupy these

empty lower energy states and emit X-rays which are characteristics of the specific element. These X-rays are detected by an X-ray detector. An X-ray spectrum is obtained which is a plot between numbers of X-rays with certain energy as a function of their X-ray energies. However, the X-rays and secondary electrons generated in the volume can themselves excite atoms and cause the emission of additional X-rays which also contribute to the EDX spectrum and needs to be taken care of in quantitative analysis.

This technique is well suited for detection of heavy elements. EDS technique can be used for point measurements, line scans as well as for area scans to obtain elemental maps.

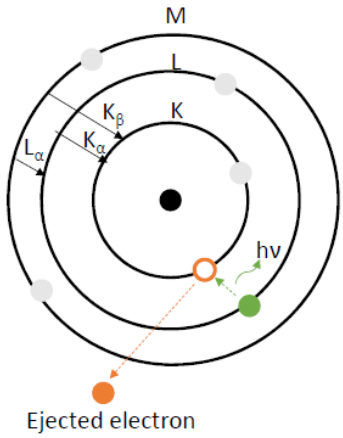

Figure 3-7: schematic of EDS

3.5.3 Electron energy loss spectroscopy (EELS)

The energy losses of electrons after passing the sample can be analyzed with electron energy-loss spectroscopy (EELS). The electron energy-loss spectrum consists

of a zero-loss peak, a low energy loss plasmon peak, and a signal background. Ionization edges which are characteristic for each element are found on top of the background. The energy resolution that can be achieved is <1 eV. This method is therefore well suited for low atomic number elements (except H and He) since scattering at low atomic number elements results in small energy losses. Therefore, EELS is complementary to EDS.

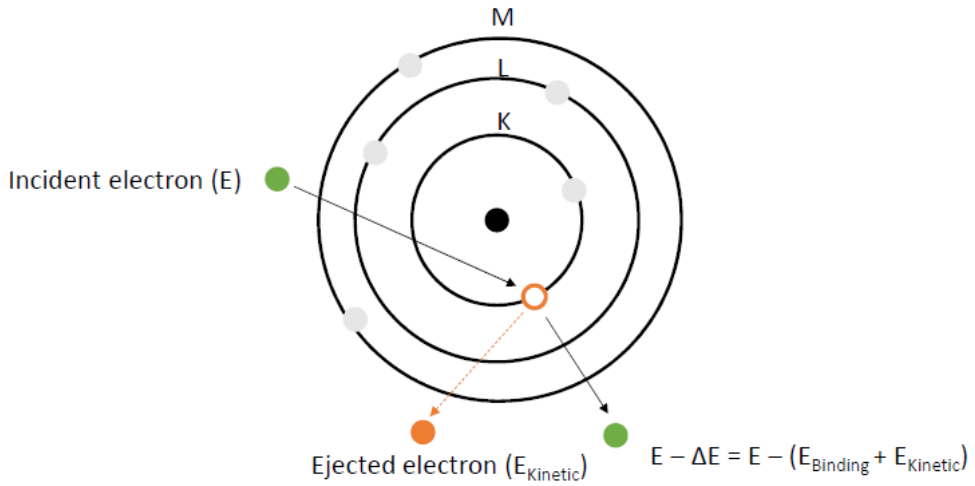

Figure 3-8: schematic of EELS

3.5.4 Energy-filtered transmission electron microscopy (EFTEM)

As describe before, EELS can be used to determine the composition on an area of interest by evaluating the ionization edges in the EELS spectrum. However, if an area of interest is imaged using only those electrons which show certain energy losses near an ionization edge then elemental maps can be obtained like EDX. This technique is known as energy-filtered transmission electron microscopy (EFTEM).

3.5.5 Energy loss near edge structure (ELNES)

When an inner shell electron undergoes a transition to the conduction band, a fine structure appears at about 30 eV from the absorption-edge in the EELS spectrum. This structure is known as energy-loss near-edge structure (ELNES). From ELNES, information about atomic bonding and oxidation states can be obtained by fingerprint method wherein the observed spectrum is compared with that of known materials.

3.5.6 Extended energy-loss fine structure (EXELFS)

When an inner shell electron that has undergone a transition to the conduction band gets scattered by the adjacent atoms, extended energy-loss fine structure (EXELFS) is obtained. It usually appears about 50 eV after ELNES. From EXELFS, information about local atomic arrangement such as co-ordination number can be obtained.

3.6 High resolution transmission electron microscopy (HRTEM)

In this technique, phase contrast is used to image lattice fringes and atomic arrangement. A very thin sample (≈ 50 nm) is required which is transparent to the incident electrons. Moreover, the sample needs to be oriented such that atomic columns are parallel to the incident electrons. As electron wave passes through a sample, there will be a phase difference between those electrons which are simply transmitted through the sample and those which undergo diffraction upon interaction with atomic columns. The

result is an interference pattern which is the HRTEM image. However, lens aberrations and sample thickness can also contribute to phase shift of electron waves, which can make the interpretation of HRTEM images difficult.

CHAPTER 4:
INFLUENCE OF SURFACE PREPARATION AND CLEANING ON THE SURFACE PASSIVATION OF SILICON SURFACES

4.1 Introduction

The recombination of charge carriers is a critical loss mechanism in crystalline silicon (c-Si) photovoltaic (PV) cells and is a good indicator of cell efficiency, everything else being equal. To minimize these losses, the effective carrier lifetime (τ_{eff}) must be high enough so that the carriers have sufficient time to reach the external circuit before they recombine. To achieve this, both bulk and surface recombination need to be minimized. Bulk recombination is limited by intrinsic properties of the material (e.g., radiative recombination, Auger recombination), as well as Shockley-Read-Hall (SRH) recombination. Auger recombination is primarily dependent on doping density, while bulk SRH recombination is dependent on material quality and can be minimized by limiting crystallographic defects, impurities, and other imperfections within the Si wafer. Surface recombination is also a form of SRH recombination, but in this case, is primarily due to the continuum of defect states arising from dangling bonds at the surface. Surface recombination can be minimized by effective surface passivation.

Therefore, in order to achieve efficiencies beyond 20% for industrially manufactured solar cells, very low surface recombination velocities are required, which can be achieved by the use of a thin dielectric films such as SiO_2, SiN_x, a-Si:H, Al_2O_3, HfO_2 [19, 23, 25, 27, 36-42] or passivation stacks like Al_2O_3/SiN_x, SiO_2/Al_2O_3, SiO_x/SiN_x, Al_2O_3/ZnO, Ta_2O_5/SiN_x.[14, 24, 43-49] Low surface recombination rates are achieved by

two methods, preferably working together: (1) reducing the fundamental surface recombination velocity of the minority carrier (S_{n0} or S_{p0}, for *p* and *n*-type materials, respectively) through a reduction of the interface defect density (D_{it}); and/or (2) reducing excess carrier concentrations near the interface via doping (i.e., surface fields) or the presence of a fixed electrostatic charge near the interface. The second mechanism is referred to as field effect passivation.

Among all passivation materials, SiN_x is the most widely used in industry because it provides both good surface passivation of phosphorus doped, n^+ emitters and has ideal optical properties for use as an antireflection coating for c-Si PV cells (e.g., transparent, appropriate refractive index). Being a positively charged dielectric, it provides excellent field effect passivation of *n*-type surfaces.[19, 39, 50] In recent years, however, researchers have shown considerable interest in Al_2O_3 as a passivation material. This is mainly due to the low D_{it} and considerable field effect passivation exhibited by Al_2O_3 on *p*-type Si surfaces, the latter attributed to the presence of a high negative charge density near the interface.[14, 23, 25, 36, 51]

The quality of surface passivation can be evaluated in terms of the measured τ_{eff}, given by the following relation:

$$\frac{1}{\tau_{eff}} = \left(\frac{1}{\tau_{rad}} + \frac{1}{\tau_{Auger}}\right) + \frac{1}{\tau_{b,SRH}} + \frac{1}{\tau_{s,SRH}} = \frac{1}{\tau_{bulk,intrinsic}} + \frac{1}{\tau_{b,SRH}} + \frac{1}{\tau_{s,SRH}} \qquad (4\text{-}1)$$

$\tau_{eff} = effective\ carrier\ lifetime$

$\tau_{rad} = carrier\ lifetime\ due\ to\ radiative\ recombination$

$\tau_{Auger} = carrier\ lifetime\ due\ to\ Auger\ recombination$

$\tau_{b,SRH} = carrier\ lifetime\ due\ to\ bulk\ defects\ i.e.\ SRH\ recombination$

$\tau_{s,SRH} = carrier\ lifetime\ due\ to\ surface\ recombination$

$\tau_{bulk,intrinsic} = intrinsic\ bulk\ carrier\ lifetime$

The surface recombination and resulting τ_{eff} of a Si wafer not only depends on the passivation material, but also on surface preparation and cleaning processes used prior to deposition. The primary cleaning processes used by the PV industry today are based on the use of HCl and HF acids, while many in the PV R&D community working on high efficiency cell architectures use more expensive and complicated cleaning processes (e.g., variants on the RCA process). As manufacturers transition from aluminum back surface field (Al-BSF) cells to rear passivated cell architectures, as predicted by the International Technology Roadmap for Photovoltaics (ITRPV)[52], (HCl + HF) cleans will not achieve the level of surface cleanliness needed and both RCA and HNO_3 cleaning processes will likely remain too expensive to implement in high-volume manufacturing. Alternative cleaning processes based on DIO_3 oxidants can provide the performance needed for high efficiency cell architectures and can potentially be inserted into high-volume manufacturing.[53, 54] Not only can DIO_3 be used to form very clean Si surfaces, but DIO_3 can be used to form very thin SiO_x layers that further reduce surface recombination.[55-60]

In this work, the influence of nine different cleaning sequences on recombination lifetime has been studied for {100} oriented *n*-type Cz -Si wafers passivated with SiN_x films and with Al_2O_3/SiN_x stacks. The passivation quality of boron diffused wafers was evaluated for both planar wafers, i.e., saw damage etch (SDE) only, and anisotropically textured wafers featuring random upright pyramids.

4.2 Experimental

In this work, 156 mm x 156 mm *n*-type {100} Cz Si wafers with a thickness of ≈195 µm and bulk resistivity of ≈3 Ω·cm were used. Processing steps were performed at Fraunhofer ISE and characterization at the University of Central Florida. All wafers were subjected to a saw damage etch (SDE), and half were subsequently anisotropically textured using an alkaline based chemistry. Half of the wafers underwent a BBr_3 tube furnace diffusion to form a ≈70 Ω/sq. p^+ emitter, and the others were left undiffused. The borosilicate glass formed on the boron diffused wafers was then removed by etching in HF solution. Each group was subjected to one of the nine cleaning sequence listed in Figure 4-1. Wafers that involved a final HF dip were collected in a single carrier and then the HF dip was performed so that the waiting time before deposition of passivation layer remains the same. HNO_3 and (HCl + HF) cleans were performed manually in a wet bench equipped with a spin rinser dryer, whereas the final HF dip and DIO_3 cleans were carried out in an automated semi-industrial wet bench featuring a blow-dryer system. After cleaning, passivation layer depositions were performed to create symmetrically passivated structures. Half of the wafers were passivated by plasma-enhanced chemical

vapor deposition (PECVD) SiN_x (≈100 nm) and the other half were passivated by a very thin Al_2O_3 film (<5 nm) deposited by spatial atomic layer deposition (ALD) followed by a PECVD SiN_x capping layer (≈100 nm). The Al_2O_3 passivated wafers were subjected to a thermal annealing step before the deposition of the SiN_x layer. Finally, each of these wafers were subjected to a simulated contact firing step to further activate the passivation layer and stay close to a potential solar cell fabrication process.

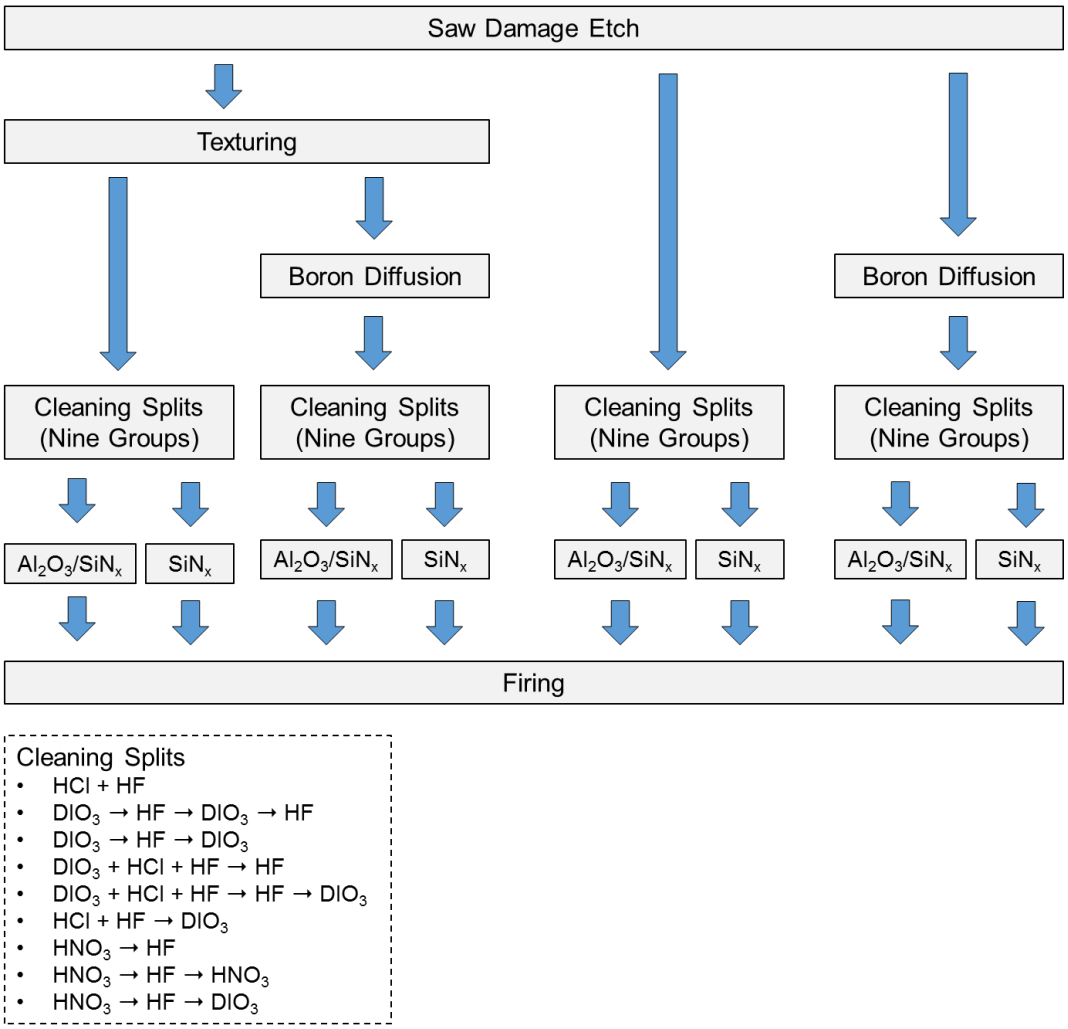

Figure 4-1: Process flow used in this work

These symmetrically passivated wafers then were characterized using the following techniques: injection-level dependent photoconductance; non-contact corona-Kelvin measurements; inductive emitter sheet resistance measurements; and secondary ion mass spectrometry (SIMS).

For the photoconductance measurements, a Sinton WCT-120 was used to measure τ_{eff} as a function of injection-level (Δn) on all wafers. For the boron diffused samples, the emitter saturation current density (J_{0E}) was extracted using a modified version of the Kane and Swanson method that accounts for bandgap narrowing.[61] The following equation was used:

$$J_{0E} = \frac{qWn_i^2}{2}\frac{d}{d\Delta n}\left(\frac{1}{\tau_{eff}} - \frac{1}{\tau_{bulk,intrinsic}}\right) \quad (4\text{-}2)$$

Where $q = fundamental\ charge$

$W = wafer\ thickness$

$n_i = intrinsic\ carrier\ concentration$

Non-contact corona-Kelvin measurements were performed on a subset of planar, undiffused wafers using a Semilab PV-2000A metrology tool and were used to extract the interface defect density near midgap ($D_{it,midgap}$) and total charge (Q_{tot}) of the dielectric film(s).[62] The sheet resistance (R_{sheet}) of the boron diffused wafers was determined by inductive coupling.[63] To determine the boron concentration in the Si wafers as a function of depth, a PHI Adept 1010 Dynamic SIMS System featuring a 300nA Cs+ ion beam at 2 keV primary energy was used. The raster size was 500 µm x 500 µm and the

detection area was 5%. The SIMS measurements were performed on six of the diffused, planar wafers just to verify a consistent dopant profile was used for all the different groups.

4.3 Results and discussion

4.3.1 Sheet resistance and boron concentration profiles

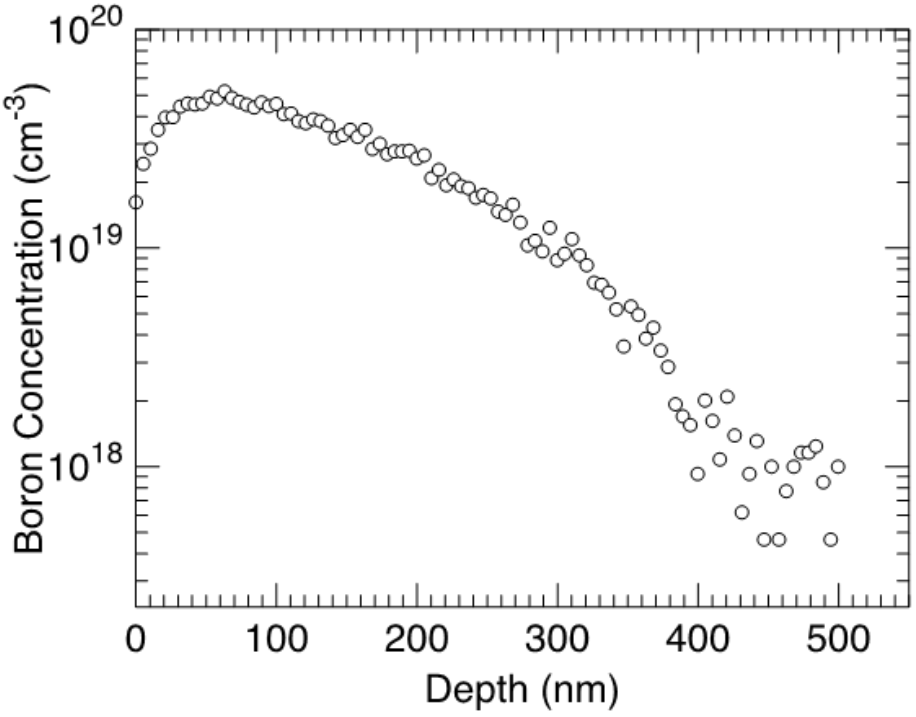

Figure 4-2: Typical boron concentration depth profile obtained by SIMS for planar wafers.

Average R_{sheet} from 108 positions was measured to be 70 Ω/sq. for the textured and 68 Ω/sq. for planar wafers. The boron concentration measured as a function of depth was found to be nearly constant for the diffused wafers. This allows for good comparisons across sub-groups without concerns of variation in recombination occurring within the

emitter itself, as opposed to the surface. Typical boron depth profile obtained by SIMS is shown in Figure 4-2.

4.3.2 Recombination characteristics

The τ_{eff} values determined at an excess carrier concentration of 10^{15} cm^{-3} are shown in Figure 4-3 for all diffused wafers, including: both planar and textured wafers; both SiN_x and Al_2O_3/SiN_x passivation; and all nine cleaning sequences. Figure 4-4(a-d) shows the $\tau_{eff}(\Delta n)$ measured for three representative cleaning sequences and the following boron diffused sub-groups: (a) planar SiN_x; (b) planar Al_2O_3/SiN_x; (c) textured SiN_x; and (d) textured Al_2O_3/SiN_x.

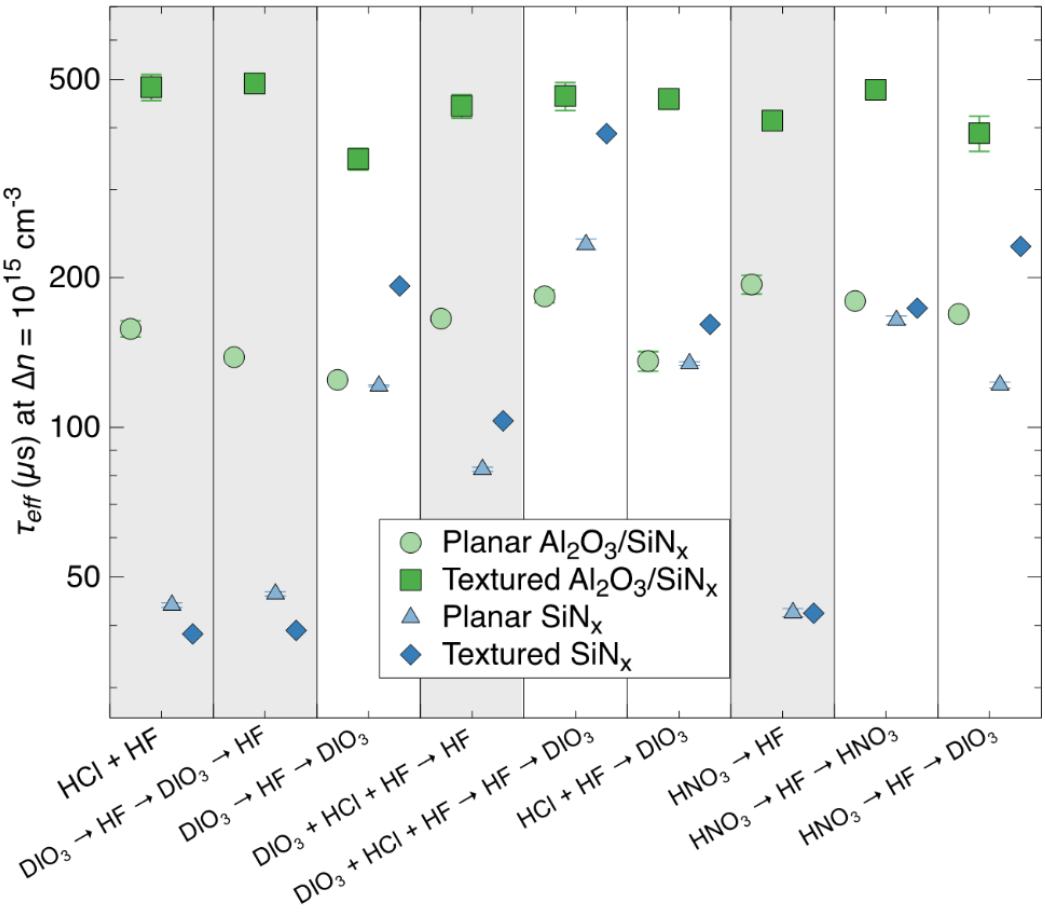

Figure 4-3: Mean τ_{eff} at $\Delta n = 10^{15}$ cm^{-3} for the boron diffused, symmetrically passivated wafers. Note, the shaded columns represent the HF last cleaning processes and the white columns oxide last. The error bars represent the standard deviation in τ_{eff} across the sample surface.

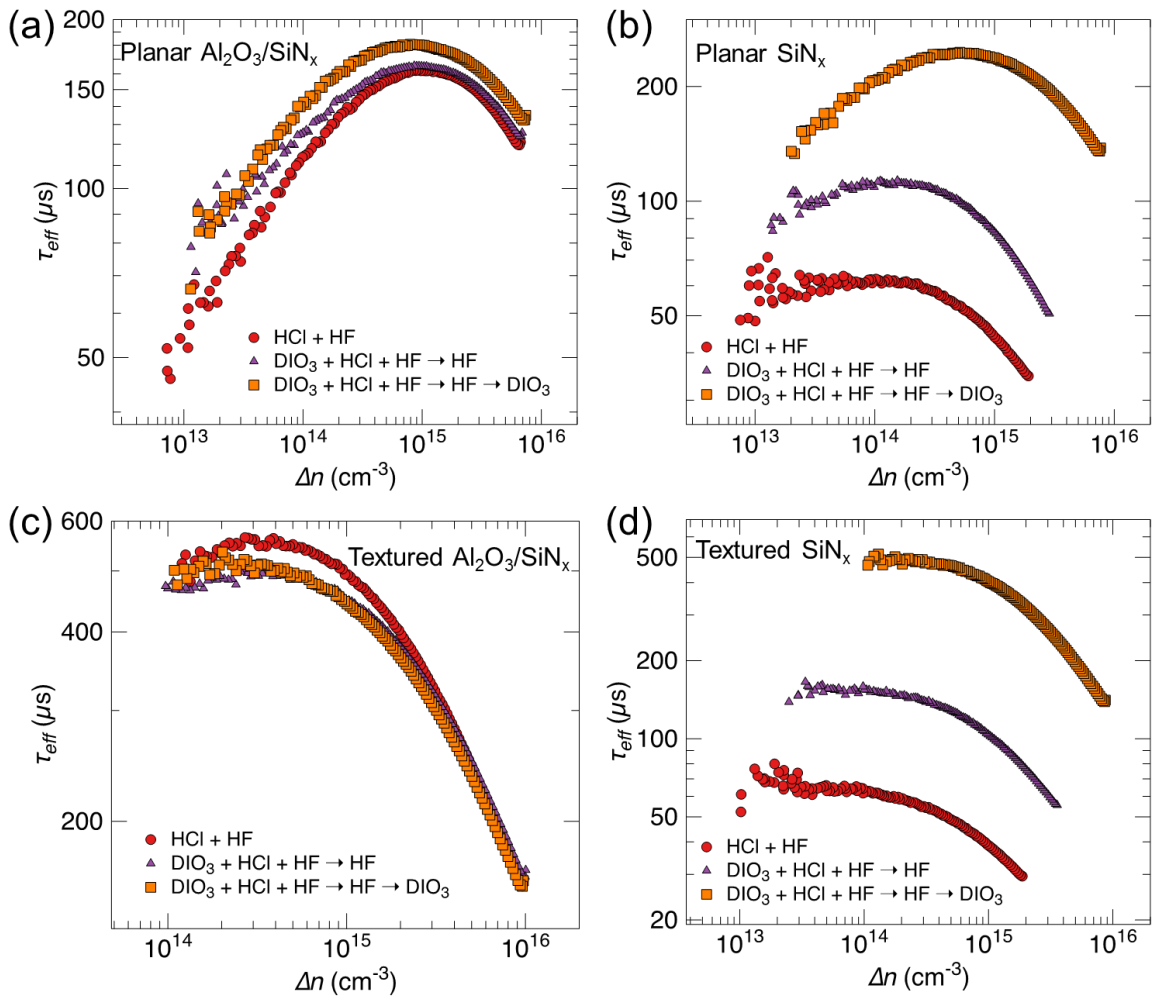

Figure 4-4: τ_{eff} as a function of Δn measured for boron diffused wafers prepared using three different cleaning sequences and featuring: (a) planar surface and Al_2O_3/SiN_x passivation; (b) planar surface and SiN_x passivation; (c) textured surface and Al_2O_3/SiN_x passivation; and (d) textured surface with SiN_x passivation. The three cleaning sequences include the industry standard (HCl+HF) clean and two very promising cleans featuring DIO_3 developed at Fraunhofer ISE, one HF last and one oxide last

In general, the Al_2O_3/SiN_x passivation stack results in higher τ_{eff} than SiN_x alone. This is consistent with prior work and thought to be due to: (1) the positive Q_{tot} at the p^+ Si/SiN_x interface, resulting in an increase in minority carriers, as opposed to the negative Q_{tot} of Al_2O_3 that reduces the concentration of minority carriers at the p^+ Si surface; and (2) the formation of defects at the p^+ Si/SiN_x interface that are not formed at phosphorus doped n^+ Si/SiN_x interfaces.[64, 65] Additionally, the variation in τ_{eff} for different cleaning sequences is much larger for the SiN_x passivated wafers than those passivated with the Al_2O_3/SiN_x stack. This is clearly illustrated in Figure 4-4, where τ_{eff} for the Al_2O_3/SiN_x passivated wafers are nearly equivalent, whereas the SiN_x passivated wafers show a large variation for each cleaning sequence.

For the planar SiN_x coated wafers, the highest values of $\tau_{eff}(10^{15}\ cm^{-3})$ are 233 µs and 164 µs for the (DIO_3+HF+HCl→HF→DIO_3) clean and (HNO_3→HF→HNO_3) clean, respectively. This is significantly higher than the 42 µs measured for standard (HCl+HF) clean. Another observable trend for the planar SiN_x passivated wafers is all of the oxide-last cleaning sequences perform better than their HF last counterparts: the $\tau_{eff}(10^{15}\ cm^{-3})$ for the (DIO_3→HF→DIO_3) clean is higher than the (DIO_3→HF→DIO_3→HF) clean; (DIO_3+HF+HCl→HF→DIO_3) is greater than (DIO_3+HF+HCl→HF); (HCl+HF→DIO_3) is greater than (HCl+HF); and HNO_3→HF→DIO_3) is greater than (HNO_3→HF). For the textured SiN_x passivated wafers, the highest measured $\tau_{eff}(10^{15}\ cm^{-3})$ are 389 µs, 192 µs, and 173 µs for the (DIO_3+HF+HCl→HF→DIO_3) clean, the (DIO_3→HF→DIO_3) clean, and the (HNO_3→HF→HNO_3) clean, respectively. Again, this is much higher than the 39 µs determined for the standard (HCl+HF) clean. As with the planar SiN_x passivated wafers,

the oxide-last treatment results in higher lifetimes than HF-last. We believe the thin SiO_x layer formed after the oxide-last treatment with either HNO_3 or DIO_3 limits the formation of defects at the p^+ Si/SiN_x interface resulting in a lower D_{it}.[59]

For both the planar and textured Al_2O_3/SiN_x passivated wafers, the impact of each cleaning sequence on τ_{eff} is much less pronounced. All of the cleaning sequences resulted in $\tau_{eff}(10^{15}\ cm^{-3})$ values above 100 µs, and surprisingly, the textured wafers outperformed the planar wafers. In prior work, it has been shown that a thin SiO_x layer forms at the Si/Al_2O_3 interface, and this interlayer is likely responsible for providing the low D_{it} values associated with this passivation material.[26, 66, 67] Moreover, the negative fixed charge at the $Si/SiO_2/Al_2O_3$ interface supports the diffusion induced repelling of minority carriers from the interface, which makes the impact of the actual D_{it} value smaller, compared to SiN_x, where a low D_{it} is needed to allow for a low surface recombination velocity. We believe therefore the Al_2O_3/SiN_x passivated wafers are relatively independent of whether an oxide-last or HF-last cleaning sequence is used.

The J_{0E} values of all the boron diffused wafers are shown in Figure 4-5. As with τ_{eff}, the resulting J_{0E} values of the SiN_x passivated wafers are heavily influenced by whether an oxide-last or HF-last cleaning sequence is used. Also in a similar fashion with τ_{eff}, the Al_2O_3/SiN_x passivated wafers appear to be practially independent of the cleaning sequence used. Notably, the (DIO_3+HF+HCl→HF→DIO_3) clean results in comparable J_{0E} values for both the SiN_x and the Al_2O_3/SiN_x passivated wafers, possibly enabling a less complex and more cost-effective alternative to Al_2O_3/SiN_x.

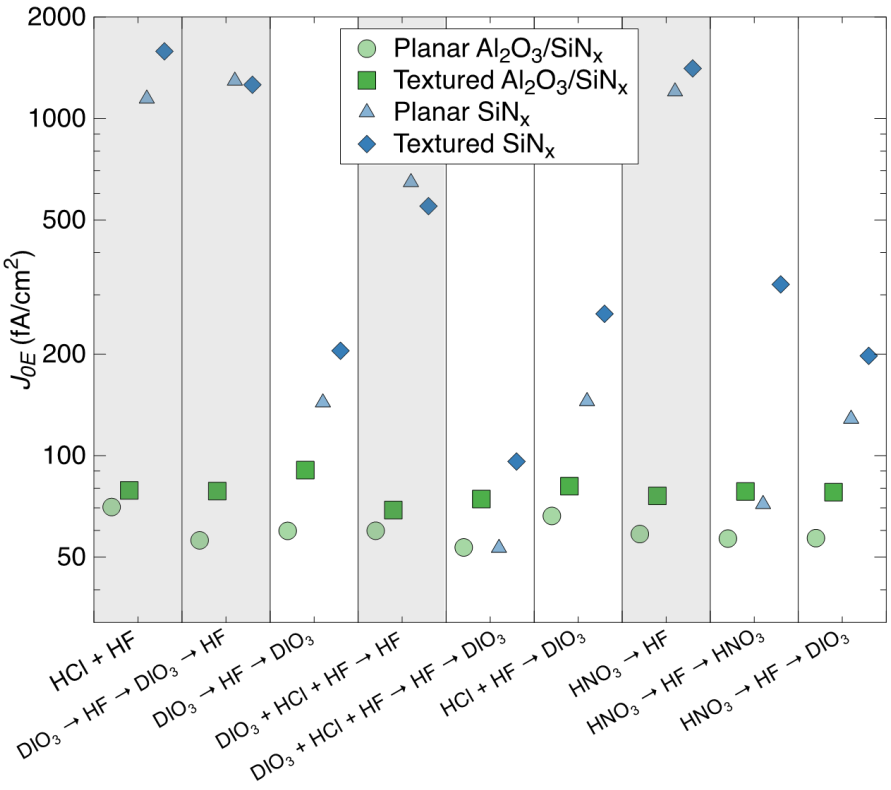

Figure 4-5: J_{0E} for the boron diffused, symmetrically passivated wafers. The shaded columns represent the HF last cleaning processes and the white columns oxide last.

4.3.3 Electronic properties of the interface

To get additional insight in the electronic properties at the Si/dielectric interface, non-contact corona-Kelvin probe measurements have been performed on undiffused, planar wafers for five cleaning sequences. The (HCl+HF) clean was selected for these measurements as a baseline, while the other four were selected due to the promising results from the photoconductance measurements. The resulting $D_{it,midgap}$ and Q_{tot} are shown in Figure 4-6. As with the τ_{eff} and J_{0E} results, here the $D_{it,midgap}$ varies widely for the

SiN_x passivated wafers, but varies little for the Al_2O_3/SiN_x passivated wafers. And again, for the SiN_x passivated wafers the oxide-last cleaning sequences give the best performance with an order of magnitude lower $D_{it,midgap}$ compared to their HF-last counterparts. The Q_{tot}, and presumably the field effect passivation, are not influenced by whether the cleaning sequence terminates with an oxide-last or HF-last step. As shown via simulation in the subsequent section, the large positive Q_{tot} for the SiN_x passivation means a very low $D_{it,midgap}$ is needed to achieve a low J_{0E}, whereas the large negative Q_{tot} of the Al_2O_3/SiN_x passivation stack is less sensitive to variations in $D_{it,midgap}$.

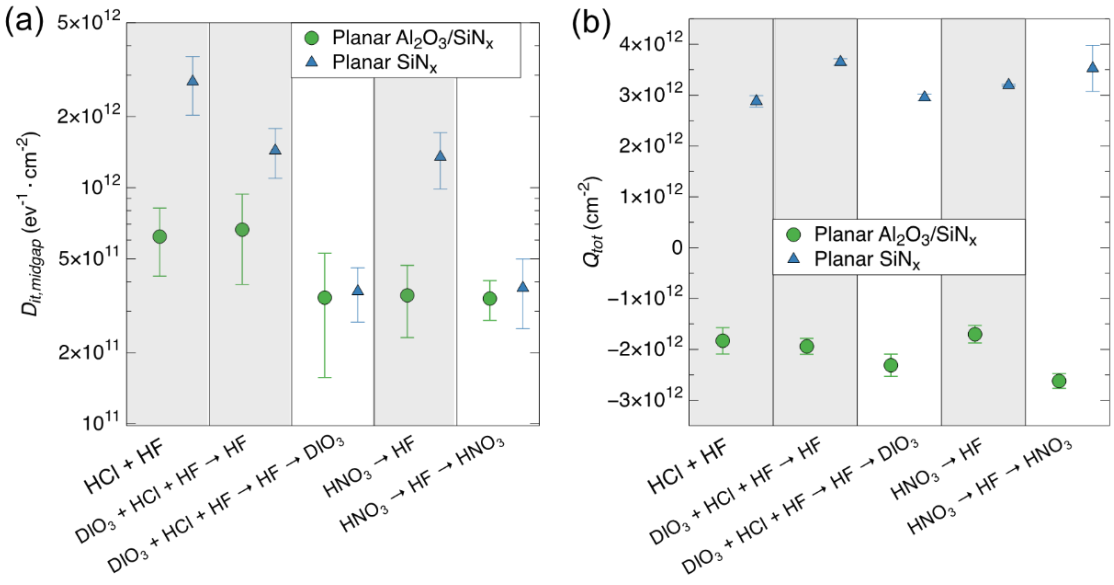

Figure 4-6: (a) $D_{it,midgap}$ and (b) Q_{tot} of undiffused, planar wafers for five different cleaning sequences. Measurements were performed on seven different locations on the wafer with error bars representing the standard deviation across the sample surface. The shaded columns represent the HF-last cleaning processes and the white columns oxide-last.

4.4 Conclusion

In conclusion, cleaning sequences featuring HNO_3 and DIO_3 and an oxide-last step resulted in better passivation quality than a (HCl+HF) clean for boron diffused and SiN_x passivated wafers. These cleaning sequences enable the dissolution of contaminants and incorporation into an SiO_x layer, which is removed using HF. The oxide-last step reduces the $D_{it,midgap}$ of SiN_x passivated wafers by almost one order of magnitude compared to similar cleaning ending with a HF-last step. The cleaning sequence used has much less of an influence on the passivation quality of the Al_2O_3/SiN_x passivated wafers. This is likely due to the known formation of a very thin SiO_x interlayer that forms at the Si/Al_2O_3 interface even on HF-last terminated cleaning sequences. For both the SiN_x and Al_2O_3/SiN_x passivated wafers studied in this work, the Q_{tot}, and therefore field effect passivation, is not influenced by the cleaning sequence. The findings in this work are applicable to any PV cell architecture featuring boron diffused surfaces, like *n*-type cells with either a front or rear p^+ emitter or *p*-type passivated emitter and rear totally diffused (PERT) cells with a p^+ BSF. The (DIO_3+HF+HCl→HF→DIO_3) cleaning sequence seems particularly promising for PV cell manufacturing, since it requires lower process temperatures than HNO_3-based cleans while still enabling high performance. In addition, it has been implemented on an automated wet bench and is ready to be transferred to industry.

CHAPTER 5:
MICROSCOPIC ORIGIN OF VARIATION IN SURFACE RECOMBINATION OF SILICON FOR DIFFERENT SURFACE PREPARATION METHODS

5.1 Introduction

In previous chapter, the influence of nine different cleaning sequences on recombination lifetime has been studied for {100} oriented *n*-type Cz -Si wafers passivated with SiN_x films and with Al_2O_3/SiN_x stacks. The passivation quality of boron diffused wafers was evaluated for both planar wafers, i.e., saw damage etch (SDE) only, and anisotropically textured wafers featuring random upright pyramids.

The study revealed that cleaning sequences featuring HNO_3 and DIO_3 and an oxide-last step resulted in better passivation quality than a (HCl+HF) clean for boron diffused and SiN_x passivated wafers. It was observed that the oxide-last step reduces the $D_{it,midgap}$ of SiN_x passivated wafers by almost one order of magnitude compared to similar cleaning ending with a HF-last step. On the other hand, the cleaning sequence used has much less of an influence on the passivation quality of the Al_2O_3/SiN_x passivated wafers. For both the SiN_x and Al_2O_3/SiN_x passivated wafers studied in this work, the Q_{tot}, and therefore field effect passivation, is not influenced by the cleaning sequence.

To understand the microscopic origin of variation in passivation performance for the various cleans as reported in prior study, wafers subjected to different cleans and passivated with either SiN_x or Al_2O_3/SiN_x were investigated using a combination of photo conductance lifetime measurement and cross-sectional TEM studies.

5.2 Experimental

156 mm x 156 mm *n*-type Cz-Si wafers were used in this work. The wafers had a thickness of ≈200 µm and a bulk resistivity of ≈3 Ω·cm. At first, the wafers were taken through a standard saw damage etch process. As noted in the flowchart in Figure 5-1, the wafers were then divided into 5 groups and each group was subjected to one of the 5 cleaning sequence which included HCl+HF clean which is the industry standard, DIO_3 cleans with HF-last and oxide-last namely DIO_3+HF+HCl→HF and DIO_3+HF+HCl→HF→DIO_3 respectively; HNO_3 cleans with HF-last and oxide-last namely HNO_3→HF and HNO_3→HF→HNO_3 respectively. Wafers going through either of the HF-last treatment were grouped after prior steps into a single carrier and subsequently the HF-last step was carried out to ensure identical wait times prior to deposition of passivation layer. HNO_3 and HCl+HF cleaning steps were performed manually in a wet bench equipped with a rinser dryer, whereas final HF and DIO_3 cleaning steps were carried out in an automated wet bench and wafers were then dried in a blow-dryer system.

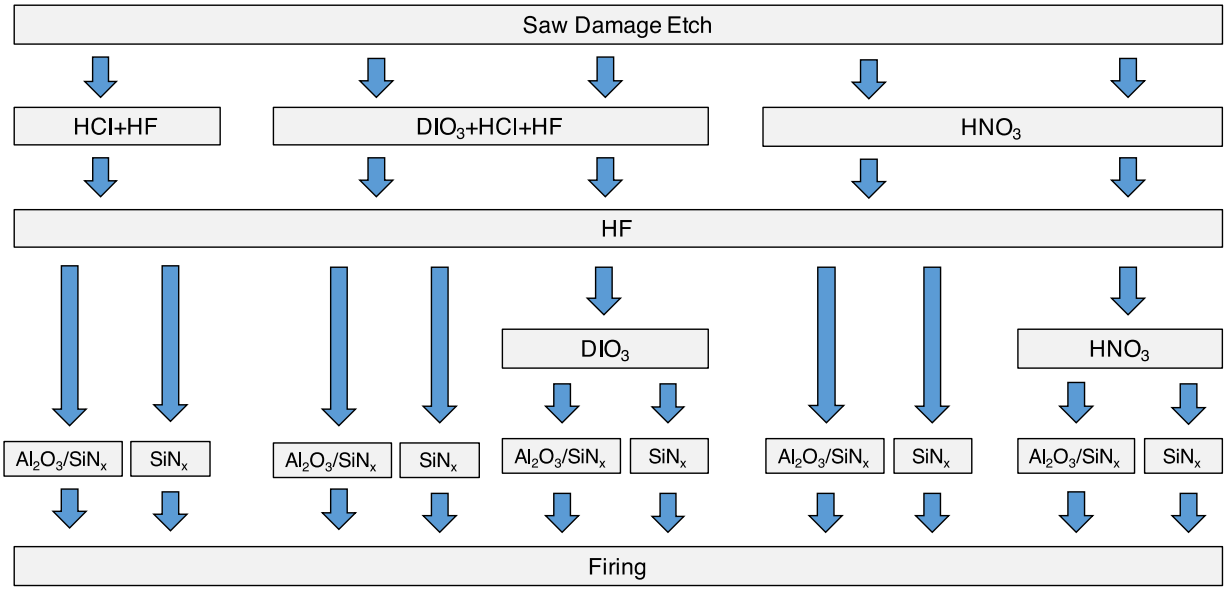

Figure 5-1: Process flow showing the surface preparation and cleaning steps, film depositions, and firing step performed before sample characterization.

After cleaning, the groups of wafers were then further subdivided based on two passivation materials. Symmetrically passivated structures were formed using plasma-enhanced chemical vapor deposition (PECVD) of SiN_x (≈100 nm) on half the wafers and by ALD of a thin Al_2O_3 (<5 nm). The wafers passivated by ALD Al_2O_3 were also subjected to thermal annealing followed by the deposition of a PECVD SiN_x film (≈100 nm). As a final processing step before characterization, all wafers were subjected to firing process to simulate the typical firing process used for screen-printed metal contacts. The symmetrically passivated test structures for SiN_x and Al_2O_3/SiN_x stacks are illustrated in Figure 5-2.

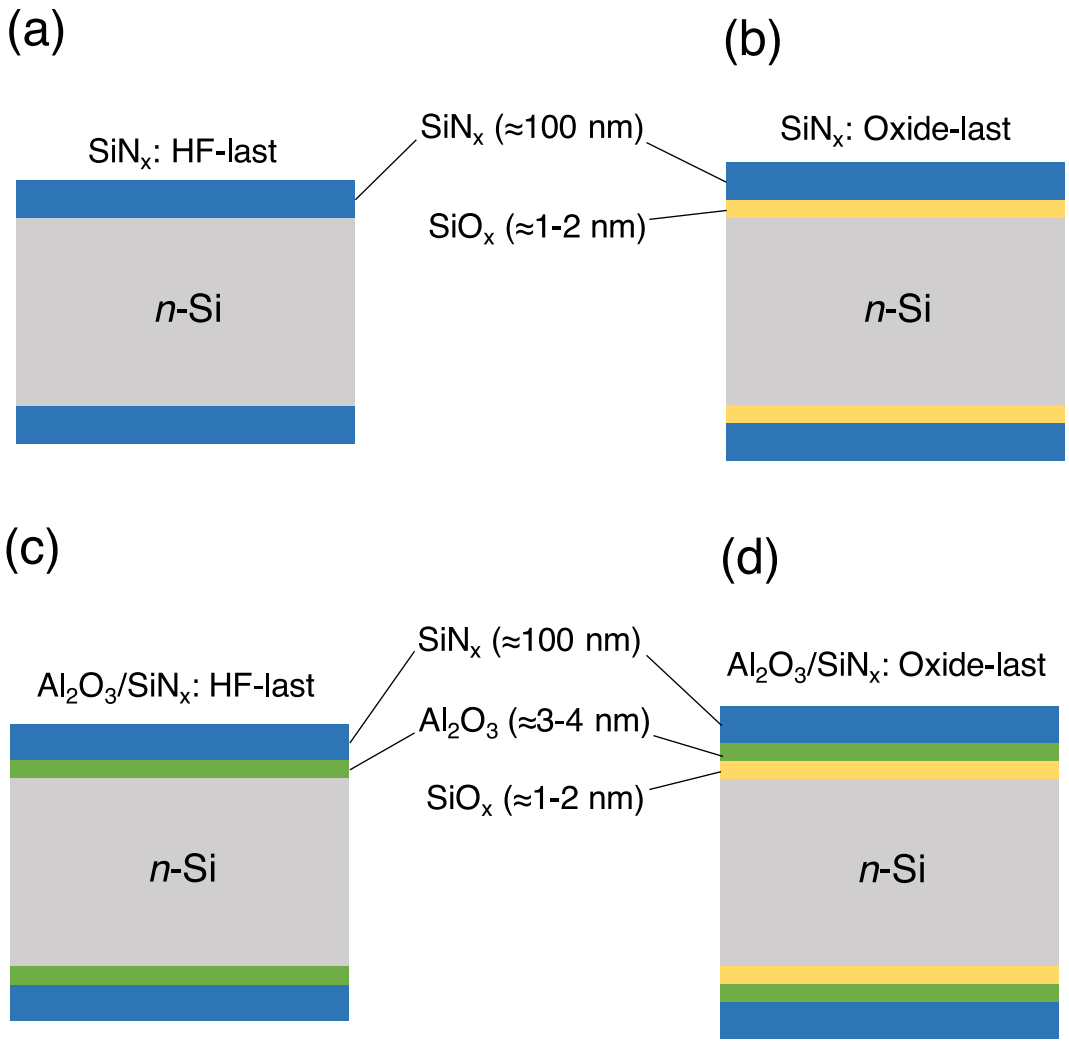

Figure 5-2: Illustration of the following symmetrically passivated test structures: (a) SiN_x with HF-last cleaning process; (b) SiN_x with oxide-last; (c) Al_2O_3/SiN_x with HF-last; and (d) Al_2O_3/SiN_x with oxide-last.

To evaluate passivation performance, effective carrier lifetime(τ_{eff}) was measured by photo conductance with the help of Sinton WCT-120 which measures τ_{eff} as a function

of injection-level (Δn). The extent of surface recombination can be measured in terms of effective surface recombination velocity is related to τ_{eff} by the relation

$$S_{eff} = \frac{W}{2}\left(\frac{1}{\tau_{eff}} - \frac{1}{\tau_b}\right) \quad (5\text{-}1)$$

$S_{eff} = Surface\ recombination\ velocity$

$W = thickness\ of\ the\ silicon\ substrate$

$\tau_{eff} = effective\ carrier\ lifetime$

$\tau_b = bulk\ recombination\ lifetime$

In this study, since high quality Si wafers were used where $\tau_b \rightarrow \infty$ and therefore equation 5-1 reduces to

$$S_{eff} = \frac{W}{2\tau_{eff}} \quad (5\text{-}2)$$

Finally, for TEM studies, cross-sectional TEM specimens were prepared by a focused ion beam (FIB) milling technique. FEI 200 TEM FIB operating at 30 KV was used for this purpose. TEM studies were performed with the help of FEI Tecnai F30 TEM. The operating voltage was kept constant at 300 KV. Z-contrast images of SiN_x and Al_2O_3/SiN_x stacks were obtained under high angle annular dark field (HAADF) conditions in scanning TEM (STEM) mode.

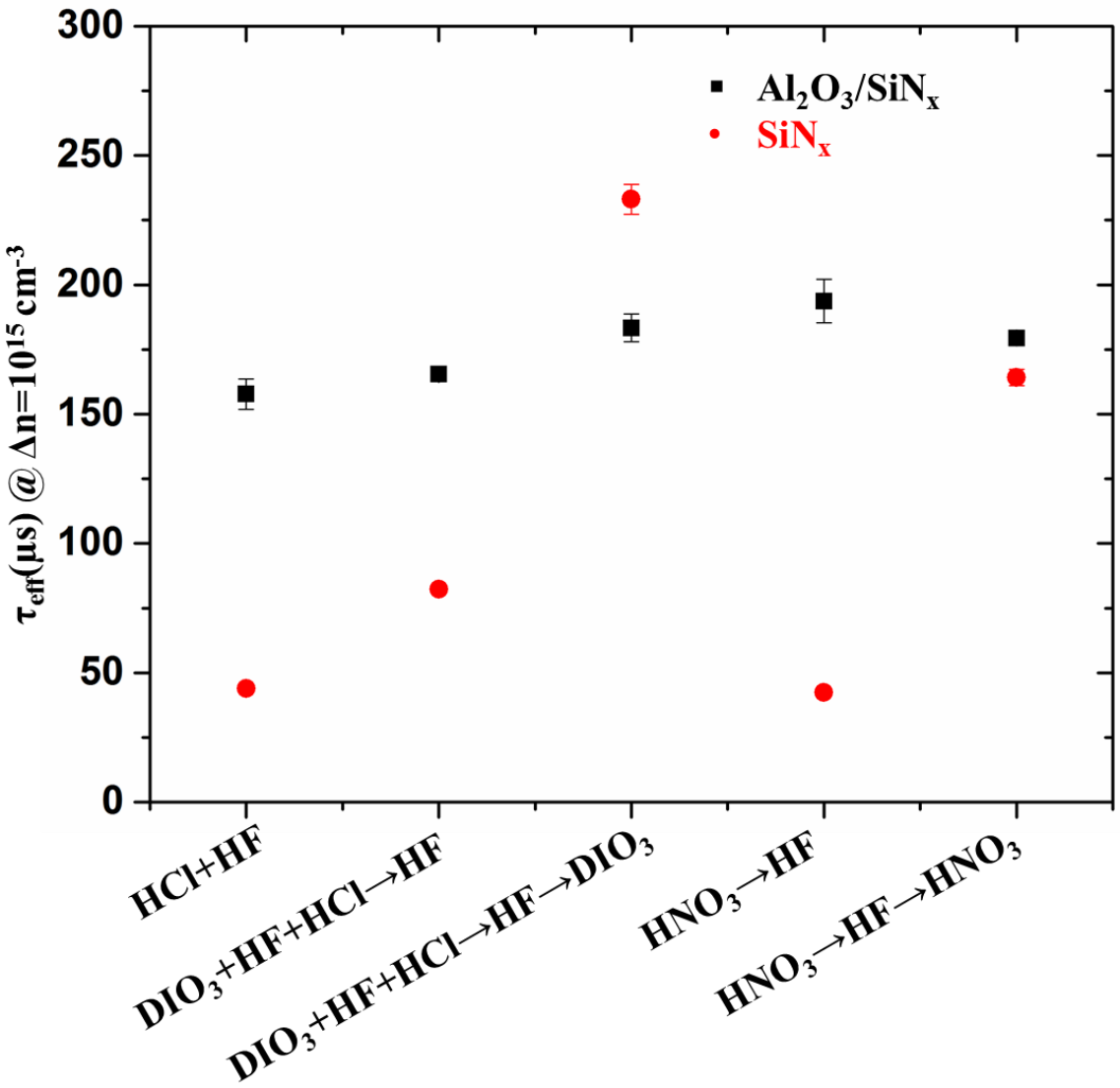

Figure 5-3: τ_{eff}(μs) @ Δn=10^{15} cm^{-3} for 5 different cleans

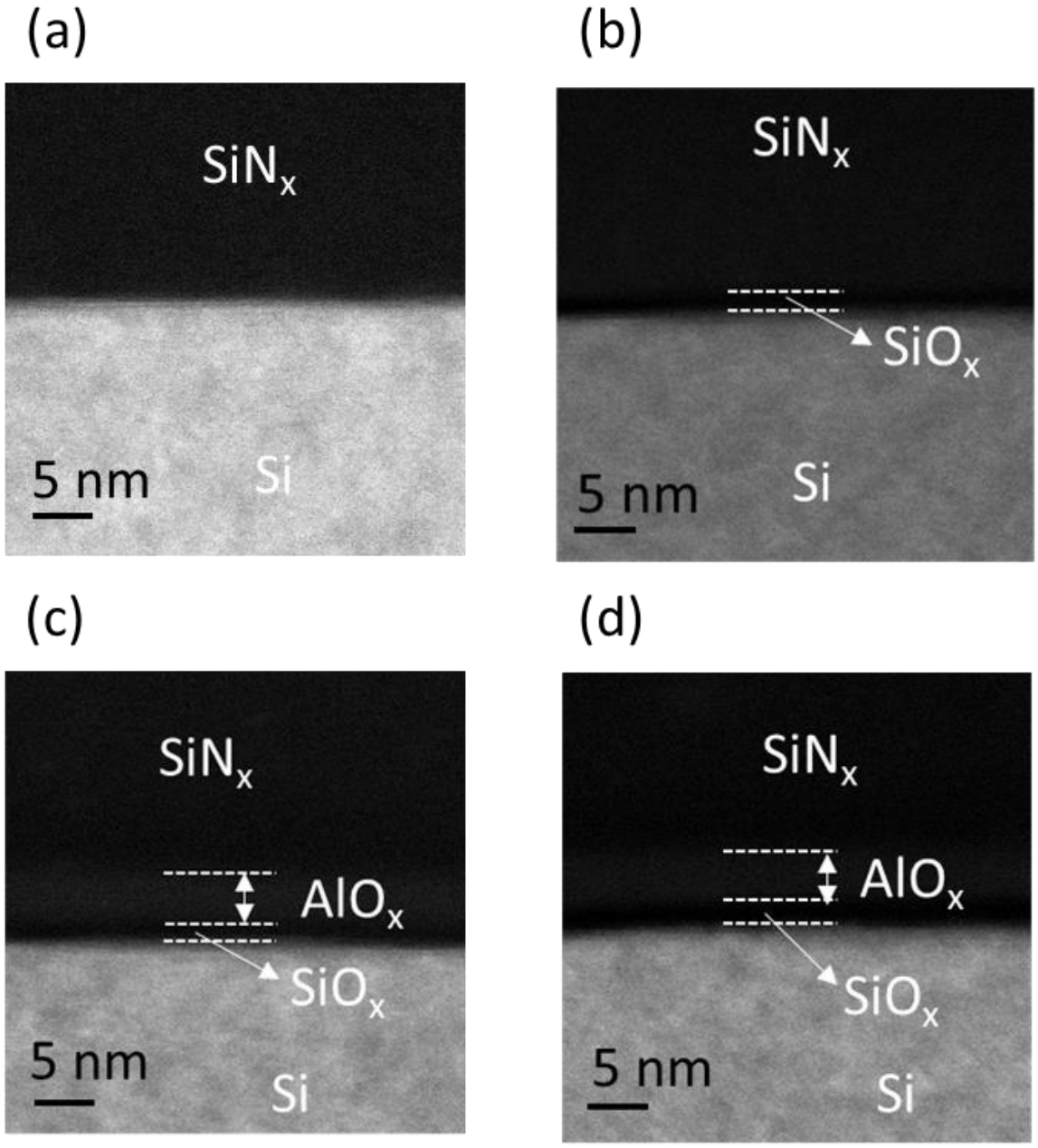

Figure 5-4: High-angle annular dark field (HAADF) images showing Z-contrast: (a) SiN_x stacks with an HF-last step; (b) SiN_x stacks with oxide-last step; (c) Al_2O_3/SiN_x stacks with HF-last step; and (d) Al_2O_3/SiN_x stacks with oxide-last step.

From Z-contrast images shown in Figure 5-4, it is evident that for SiN_x stacks, an ultra-thin (1-2 nm) SiO_x layer is present if the cleans involved an oxide-last step whereas no SiO_x layer is observed for cleans that with a HF-last step. Further, DIO_3+HF+HCl→HF→DIO_3 and HNO_3→HF→HNO_3 cleans which involve an oxide-last step results in much higher τ_{eff} values as compared to DIO_3+HF+HCl→HF, HNO_3→HF and HCl+HF cleans which have an HF-last step as shown in Figure 5-3. It has previously been reported that a wet-chemically grown SiO_x interlayer leads to higher effective carrier lifetimes due to a significant reduction in $D_{it,midgap}$.[56, 58, 59] Therefore, we can conclude that the higher lifetimes obtained for DIO_3+HF+HCl→HF→DIO_3 and HNO_3→HF→HNO_3 cleans is due to the chemical passivation exhibited by the 1-2 nm SiO_x layer formed as a result of oxide-last step during wafer cleaning process.

On the other hand, it can be observed from Z-contrast images of Al_2O_3/SiN_x stacks shown in Figure 5-4 that a SiO_x layer is present regardless of whether clean involves oxide-last or HF-last step. This indicates that even if no oxide-last step is involved during wafer cleaning prior to Al_2O_3 deposition, SiO_x will eventually be grown possibly when Si substrate is exposed to oxygen during first ALD cycles.[26] This explains why the impact of clean on chemical passivation and consequently on carrier lifetime in case Al_2O_3/SiN_x stacks is not significant as evident in Figure 3. Moreover, excellent field effect passivation of Al_2O_3 due to the presence of negative fixed charges plays a major role in passivation performance of Al_2O_3/SiN_x stacks which is not dependent on the presence of SiO_x layer.

Furthermore, it can be seen from τ_{eff} maps in Figure 5-3 that carrier lifetimes obtained with SiN_x stacks having an oxide-last cleaning step is comparable to or even higher than that obtained with Al_2O_3/SiN_x stacks. Moreover, TEM images revealed that the higher lifetimes obtained for SiN_x stacks having an oxide-last step is due to the presence of an ultra-thin SiO_x layer. This indicates that excellent carrier lifetimes with SiN_x stacks can possibly be obtained by having a wet chemical treatment of Si wafers to grow a tunnel SiO_x layer prior to deposition of SiN_x by PE-CVD. Such a wet chemical treatment process is attractive since it doesn't require high temperatures (≈900 °C) nor the costs associated with deposition of a SiO_2 layer by thermal oxidation.

5.4 Conclusion

In summary, this study has revealed that in case of Al_2O_3/SiN_x stacks, 1-2 nm SiO_x is present regardless of whether cleaning procedure terminates with a HF-last or oxide last step which is why the cleaning procedure doesn't impact the passivation performance of Al_2O_3/SiN_x stacks. However, in case of SiN_x stacks, it was observed that an oxide-last cleaning step to form a 1-2 nm SiO_x layer prior to deposition of SiN_x is essential for obtaining results in excellent carrier lifetimes. Overall, it emerged that SiO_x/SiN_x stacks consisting of a chemically grown ultra-thin SiO_x layer with SiN_x as a capping layer are potential candidates for use as passivation layers in c-Si solar cells. Moreover, SiN_x acts as an excellent anti-reflection coating(ARC) and is widely used in photovoltaics industry and therefore SiO_x/SiN_x stacks can provide excellent anti-reflection properties as well as carrier lifetimes simultaneously.

CHAPTER 6:
TITANIUM OXIDE AS A ELECTRON-SELECTIVE REAR CONTACT FOR N-TYPE CRYSTALLINE SILICON SOLAR CELL

6.1 Introduction

It has already been discussed that low recombination velocities at surface is essential for obtaining higher efficiencies for c-Si solar cells. One of the techniques employed for this purpose is the use of carrier selective contacts. CSCs not only passivate the silicon surface but are also carrier-selective in nature i.e. they only allow either electrons or holes to pass through. The incorporation of CSCs into silicon solar cell improves cell efficiency by providing excellent surface passivation at both contact and noncontact regions resulting in a high open-circuit voltage V_{OC}, and lower contact resistance resulting in a high fill factor FF.[21, 68-70]

Typically, a CSC can be achieved by deposition of conducting layer over an ultra-thin passivation layer. For instance, a stack of ultra-thin SiO_2 and hydrogenated amorphous silicon a-Si:H(n) can act as an electron-selective layer whereas SiO_2/a-Si:H(p) stack is hole-selective. Although higher efficiencies have been achieved for solar cells with CSCs based on a-Si:H and SiO_2, they suffer from certain drawbacks that include thermal instability and parasitic photon absorption of a-Si:H films, complicated deposition process, and high fabrication cost.[29, 40-42, 71]

Recently, transition metal oxides have emerged as potential alternative to a-Si:H for use as CSCs in c-Si solar cells. Typically, these CSC contain an ultra-thin layer of

metal oxide which act as electron-blocking or hole-blocking layer. For instance, TiO_2 can act as hole-blocking layer due to a small conduction band offset ($\Delta E_c \approx 0.05$ eV), which allows electrons to pass through the TiO_2 layer and a large valence-band offset ($\Delta E_v \approx 2.0$ eV), which results in holes being blocked. Recently, solar cells based on TiO_2-based electron selective contacts are gaining considerable attention. Yang et al. demonstrated that cell efficiencies upto 21.6% can be achieved for a n-type Si solar cell with a full area TiO_2/SiO_2 rear contact which is the highest reported efficiency so far for a TiO_2-based rear contact Si solar cell. [29, 72]

Although CSCs based c-Si solar cells have achieved very high efficiencies, the underlying mechanisms responsible for excellent performance of these CSCs is yet to be fully understood. In the present work, n-type Si solar cells featuring a-Si/TiO_2 rear contacts were investigated and its performance compared with that of cell devices having SiO_2/TiO_2 rear contacts. Furthermore, microscopic studies were carried out with the help of high resolution TEM (HRTEM) and analytical TEM including energy-filtered TEM techniques to understand their behavior at microscopic scale and correlate it with device performance.

6.2 Experimental

6.2.1 Device fabrication

Silicon solar cells featuring a full-area a-SiO_2/TiO_2 rear contact were fabricated on n-type c-Si wafers (1.0 Ω cm, ≈175 μm). After surface damage etching in alkaline solution,

a mask SiN_x layer (≈100 nm) was grown by low-pressure chemical vapor deposition (LPCVD) on both sides. The cell area (2 cm × 2 cm) was then realized by photolithographically defined mesa etch. Following alkaline-based surface texturing and standard RCA cleaning, a boron diffusion was performed in a clean quartz furnace, resulting in a p+ emitter with a sheet resistance of ≈120 Ω sq−1. An Al_2O_3/SiN_x stack, which was deposited by plasma ALD (Al_2O_3 ≈20 nm) and plasma enhanced chemical vapor deposition (PECVD SiN*x*, ≈50 nm), was used to passivate the front emitter. The rear TiO_2 contact was formed by depositing a TiO_2 film and evaporating an Al/Ag (20/2000 nm) stack. Cells featuring a full-area SiO_2/TiO_2 contact were subjected to a short thermal oxidation at 700 °C for 150 s for tunnel SiO_2 growth before TiO_2 films deposition. The front fingers were prepared with photolithography in combination with an evaporated stack of Cr/Pd/Ag (40/40/40 nm) that was thickened with Ag electroplating. Finally, the cells were subjected to a FGA annealing before cutting by laser for *I*–*V* measurements.

In this study, ultra-thin TiO_2 films (<5 nm) were deposited by ALD (TFS 200, BENEQ, Finland) on (100) n-type Si wafers. For ALD process, $TiCl_4$ was used as Ti precursor, H_2O as oxidant, N_2 as purge gas and deposition temperature was 75°C.

For comparison purposes, $Al/TiO_2/SiO_2$ structures were fabricated for TEM studies. For this purpose, prior to TiO_2 deposition, samples were subject to thermal oxidation in a preheated quartz tube furnace at 700 °C for only 150 s in O_2 atmosphere to allow an ultra-thin SiO_2 (<2 nm) layer to grow. Finally, Al contacts (≈2-3 µm) were formed over TiO_2 layer by evaporation.

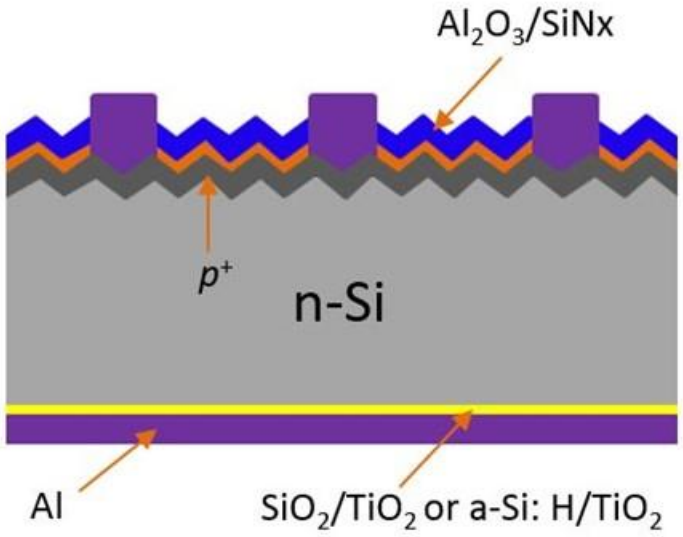

Figure 6-1: Cross-sectional illustrations of the c-Si cell with a Al/TiO_2/SiO_2 or Al/TiO_2/a-Si:H(*i*) rear contact

Figure 6-1 shows the structure of n-type silicon solar cells featuring a full-area Al/TiO_2/SiO_2 or Al/TiO_2/a-Si:H(*i*) rear contact. The textured front side with random pyramids has a boron diffused *p*+ emitter, which was passivated by Al_2O_3 /SiN_x stack. The front fingers were prepared by thermal evaporation of a Cr/Pd/Ag seed layer and subsequent electroplating of Ag.

6.2.2 Device characterization

To evaluate passivation performance, effective carrier lifetime(τ_{eff}) was measured by photo conductance. The extent of surface recombination can be measured in terms of effective surface recombination velocity is related to τ_{eff} by the relation

$$S_{eff} = \frac{W}{2}\left(\frac{1}{\tau_{eff}} - \frac{1}{\tau_b}\right) \quad (6\text{-}1)$$

$S_{eff} = Surface\ recombination\ velocity$

$W = thickness\ of\ the\ silicon\ substrate$

$\tau_{eff} = effective\ carrier\ lifetime$

$\tau_b = bulk\ recombination\ lifetime$

In this study, since high quality Si wafers were used where $\tau_b \rightarrow \infty$ and therefore equation 1 reduces to

$$S_{eff} = \frac{W}{2\tau_{eff}} \quad (6\text{-}2)$$

The *I–V* characteristics of the solar cells were measured using a Xenon-lamp solar simulator under standard 1 sun conditions (100 mW cm^{-2}, AM 1.5 spectrum, 25 °C), which was calibrated using a certified reference cell from Fraunhofer ISE CalLab.

For TEM studies, cross-sectional TEM specimens were prepared by focused ion beam (FIB) milling technique and with the help of FEI 200 TEM FIB. Specimen lift-out was done in-situ and attached to Cu gird. TEM studies were performed with the help of FEI Tecnai F 30 TEM under operating voltage of 300 KV. Cross-sectional micrographs were obtained under bright field (BF) and high resolution transmission electron microscopy (HRTEM) conditions with a point-to-point resolution of 0.2 nm. Compositional analysis was carried out with the help of electron energy loss spectroscopy (EELS) technique, since EELS is well suited for low atomic number elements. Gatan image filter

model 200 (GIF 200) spectrometer was used for this purpose. Elemental maps were obtained by energy-filtered transmission electron microscopy (EFTEM).

6.3 Results and discussion

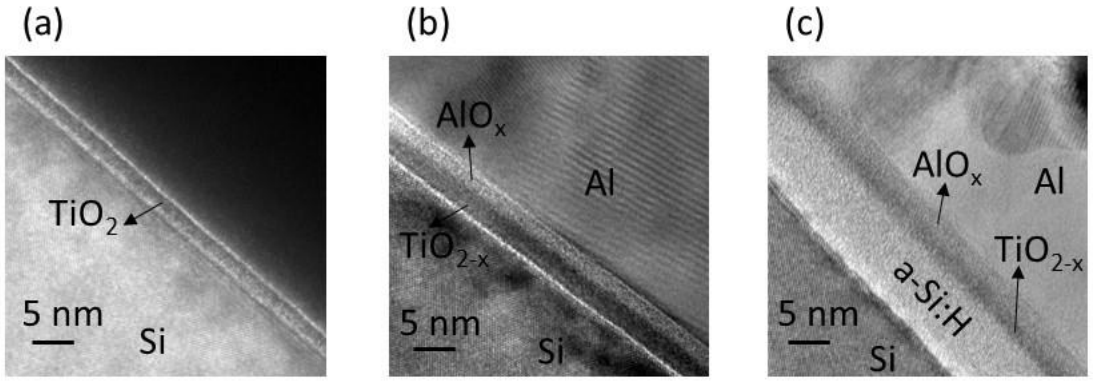

Figure 6-2: high resolution TEM (HRTEM) images of (a) as-deposited TiO_2 over Si, (b) after Al deposition, (c) Al/TiO_2/a-Si:H stack

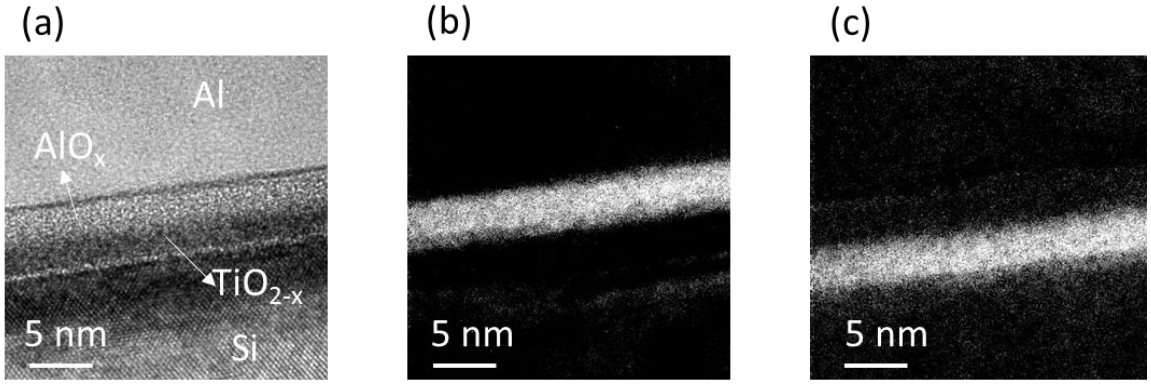

Figure 6-3: (a) high-resolution TEM (HRTEM) image of Al/TiO_2 stack; (b) and (c) EFTEM elemental map of O and Ti resp.

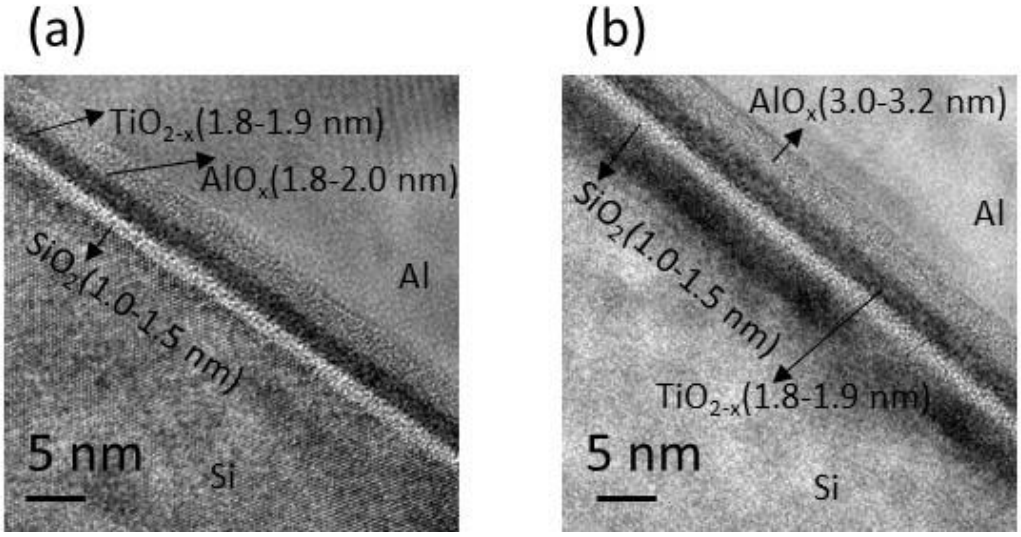

Figure 6-4: high resolution TEM (HRTEM) images of Al/TiO_2/SiO_2 stack (a)before FGA, (b) after FGA

Table 6-1: Cell parameters of n-type Al/TiO_2/SiO_2 rear contact cell

	V_{oc} (mV)	J_{sc} (mA/cm^2)	*FF* (%)	η (%)
Before FGA	650	38.2	65.6	16.3
After FGA	676	39.6	80.7	21.6

It can be seen from Figure 6-2 that an interlayer is formed Al/TiO_2 interface. This interlayer formation takes place during metallization process wherein Al is deposited over

TiO_2 by thermal evaporation.[73] Moreover, from EFTEM elemental maps of O and Ti shown in Figure 6-3, it can be inferred that oxygen has diffused from TiO_2 layer across the Al/TiO_2 interface towards Al resulting in a AlO_x interlayer and an oxygen-deficient TiO_{2-x} phase having a high concentration of vacant oxygen sites. This can be attributed to the relatively higher oxygen affinity of Al relative to Ti. Furthermore, it is evident from Figure 6-4 that thickness of AlO_x interlayer increases after FGA which indicates that further oxygen diffusion takes from TiO_{2-x} phase towards AlO_x and TiO_{2-x} becomes even more oxygen-deficient. Thus, upon FGA at 350°C, TiO_{2-x} phase has a high concentration of oxygen vacancies which significantly increases its conductivity and reduces overall rear contact resistivity and FF improves from 65.6 % to 80.7%. Although, increase in concentration of oxygen vacancies in TiO_{2-x} upon FGA is expected to degrade the passivation performance of titanium oxide phase, V_{oc} increases from 650 mV to 676 mV which can be attributed to the excellent thermal stability and improved surface passivation of 1-2 nm SiO_2 layer upon FGA at 350°C.

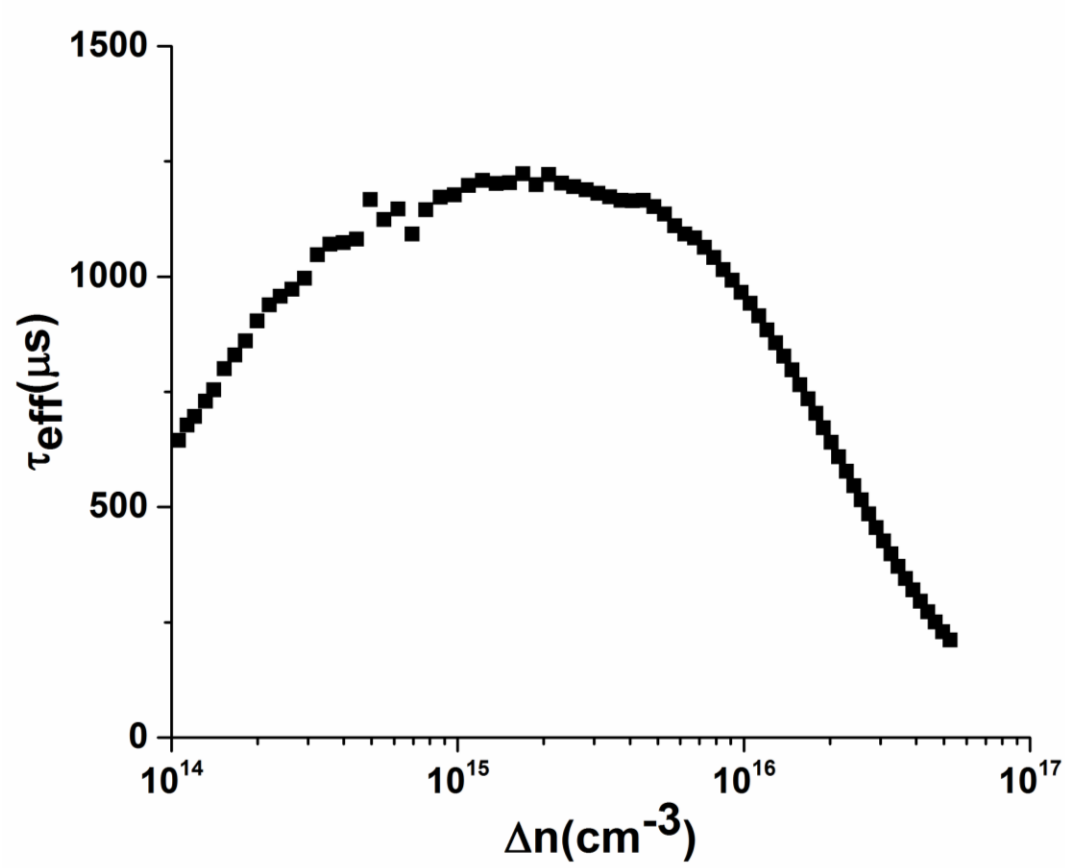

Figure 6-5: τ_{eff} as a function of Δn for as-deposited a-Si:H/TiO_2 stack

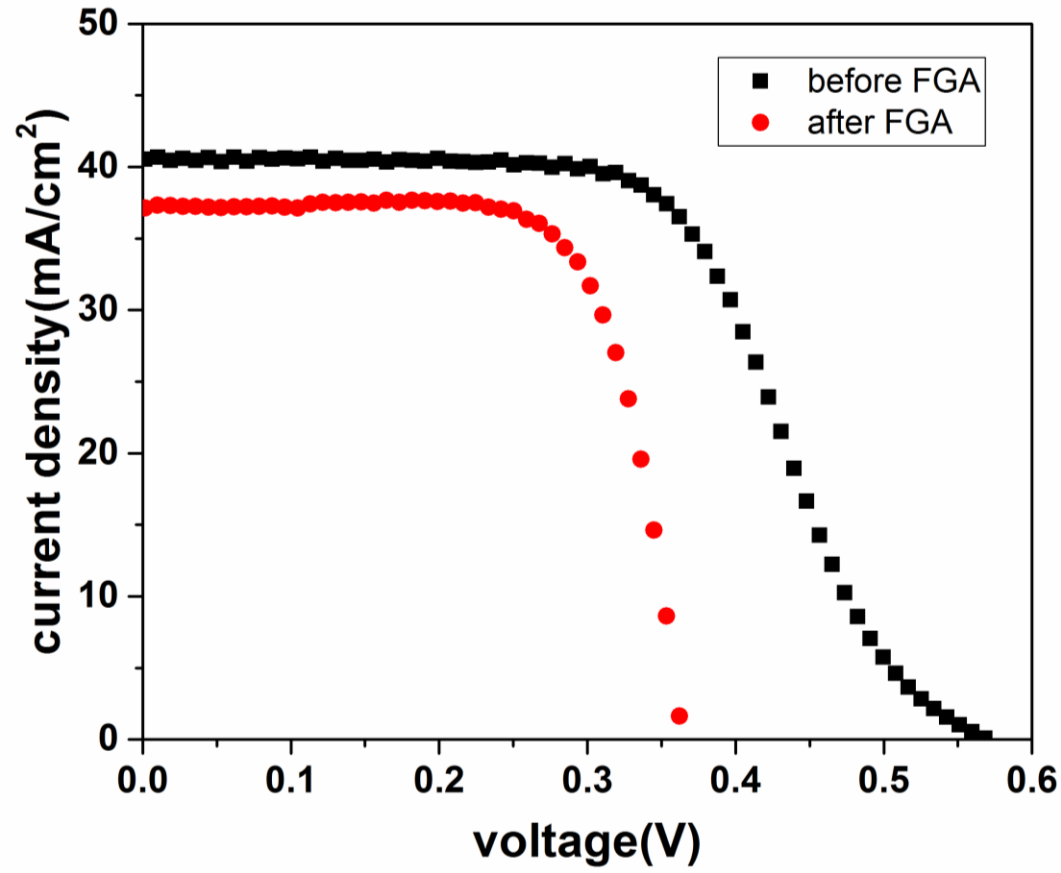

Figure 6-6: J-V characteristics of n-type cell featuring Al/TiO_2/a-Si:H rear contact

It is evident from Figure 6-5 that excellent carrier lifetimes (τ_{eff} >1ms) can be obtained with a-Si/TiO_2 stack. S_{eff} ($\Delta n=10^{15}$ cm^{-3}) and implied V_{oc} were calculated and values were found out to be 10 cm/s and 698 mV respectively. However, device performance of cells featuring a-Si:H/TiO_2 rear contact prior to anneal was much lower than expected. J-V measurement of cells prior to annealing revealed a S-shape curve with a cell efficiency of 13.2%, V_{oc} of 570 mV and a much lower FF of 57%. As already discussed, Al and TiO_2 interact during thermal evaporation of Al over TiO_2 resulting in formation of oxygen-deficient TiO_{2-x} phase and AlO_x interlayer. The field effect passivation

of titanium oxide phase is degraded due to presence of oxygen vacancies whereas reaction with Al reduces its thickness leading to degradation of its hole-blocking ability due to tunneling resulting in a lower V_{oc}.[29, 73, 74] Moreover, reduction in contact resistivity due to presence of oxygen vacancies in TiO_{2-x} is more than offset by the lower mobility of charge carriers in a-Si:H(i) which is two orders of magnitude lower compared to c-Si. The net effect is a significant increase in the rear contact resistivity which results in a much lower FF.

On the other hand, cell efficiency further drops to 9.8% upon FGA at 350°C for 30 min with a much lower V_{oc} of 365 mV but the FF improves significantly to 71.7%. It is well known that surface passivation exhibited by a-Si:H is due to hydrogen diffusion towards the a-Si:H/c-Si where it saturates the Si dangling bonds. Upon annealing at 350°C, surface passivation of a-Si:H degrades rapidly due to hydrogen evolution leading to generation of defect states resulting in a much lower τ_{eff} value. [75, 76] Thus, much lower V_{oc} of 365 mV is obtained. However, generation of defect states improves conductivity of a-Si:H which reduces overall contact resistivity and consequently FF improves from 57% to 71.7% upon FGA.

6.4 Conclusion

In a nutshell, the low efficiency of 9.8% for cells featuring a-Si:H/TiO_2 rear contact can be attributed to rapid degradation of surface passivation of a-Si:H upon FGA at 350°C due to hydrogen evolution leading to generation of defect states which increases

recombination and hence a much lower V_{oc} of 365 mV is obtained. On the other hand, 21.6% efficiency for cells featuring SiO_2/TiO_2 rear contact is due to excellent passivation of SiO_2/TiO_2 stack upon FGA anneal which can be attributed to the presence of 1-2 nm SiO_2 layer whose passivation performance improves upon FGA at 350°C whereas presence of large number of oxygen vacancies in TiO_{2-x} reduces rear contact resistivity.

CHAPTER 7:
MOLYBDENUM OXIDE AS A HOLE-SELECTIVE FRONT CONTACT FOR N-TYPE CRYSTALLINE SILICON SOLAR CELL

7.1 Introduction

It has already been discussed that to achieve excellent surface passivation as well as carrier-selectivity at the front and rear contacts, carrier selective contacts (CSCs) are employed. For an n-type c-Si solar cell, electrons and holes are to be collected from rear and front contacts respectively so it is essential to have hole-blocking and electron-blocking layers at rear and front contact regions respectively.[68] In previous chapter, TiO_2-based electron-selective rear contact for a n-type c-Si cell was investigated. In this chapter, a similar study carried out for MoO_x-based hole-selective front contacts for a n-type cell will be presented here.

As discussed before, any CSC consists of a conducting layer deposited over an ultra-thin passivation layer. Depending on the band-offset, the conducting layer can be either electron-selective or hole selective. A large valence band offset and a small conduction band offset results in holes being blocked whereas a large conduction band offset results in electrons being blocked. One of the commonly employed hole-selective CSCs consists of a stack of ultra-thin SiO_2 and doped hydrogenated amorphous silicon (a-Si:H). Alternatively, transition metal oxides have emerged as potential candidates for CSCs in c-Si solar cells. Typically, sub-stoichiometric metal oxides having a wide gap and high work function can act as electron-blocking layer due to large conduction band offset. Examples include tungsten oxide (WO_x), vanadium oxide(VO_x) and molybdenum oxide

(MoO_x). Often, these oxides are either used to replace p-type a-Si:H front contact of a standard SHJ cell or act as an additional contact layer between a-Si:H and TCO such as ITO.[21, 30-33, 68, 69, 71, 77]

Among all oxide materials investigated for hole-selective contacts on a c-Si solar cell, molybdenum oxide appears very promising. MoO_3 is a wide band gap (3 eV) material with a large work function (6.6 eV) which leads to a large conduction band offset with silicon and makes it an electron-blocking layer. Moreover, wide band gap of MoO_3 make it suitable to act as a suitable front contact. Furthermore, it can be deposited with relative ease by vacuum evaporation from a solid MoO_3 source results in a sub-stoichiometric (MoO_x, $x<3$) amorphous film. This leads formation of oxygen vacancies in MoO_x and imparts it a semi-metallic and n-type character. [32]

Although cell efficiencies upto 22.5 % have been achieved with silicon heterojunction solar cells featuring a front contact wherein MoO_x is inserted between a-Si(i) and hydrogenated indium oxide(IO:H), device performance and FF in particular degrades upon annealing beyond 130°C.[78] This is undesirable since annealing at 200°C is required for curing of Ag front contacts. The objective of the present study is to investigate the factors responsible for degradation of device performance of silicon heterojunction solar cells featuring MoO_x front contacts upon annealing. In this work, contact resistivity measurements were carried out prior to and after annealing by TLM technique followed by TEM studies including high-resolution and analytical TEM.

7.2 Experimental

In this work, p-type {100} Si was used as substrate. 5-10 nm of MoOx was deposited on Si substrate under vacuum by thermal evaporation using a solid MoO_3 source. Then, 50 nm thick transparent conducting oxide (TCO) layer of Indium Tin Oxide (ITO) was deposited over MoO_x by sputtering in Ar atmosphere at room temperature. Select samples were then annealed in air at 200°C for 30 min.

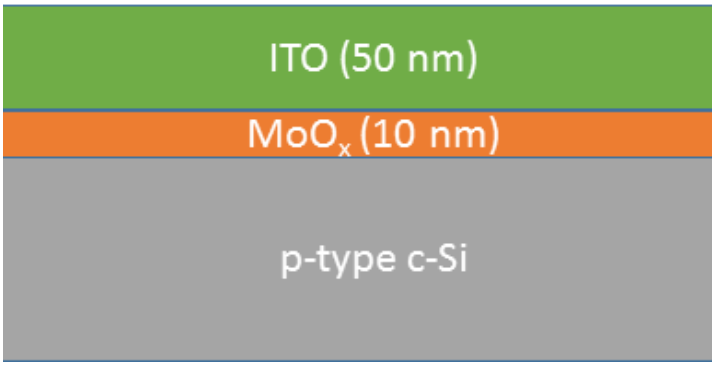

Figure 7-1: schematic of test structure

Contact resistivity measurements for both pre- and post-annealed samples were carried out by transmission line measurement (TLM) technique. TLM was used to measure the lumped contact resistivity of each passivated structure. A Keithley 2400 Sourcemeter® was used in combination with a microprobing station to the measure the total resistance R_T of each TLM contact pair. In order to obtain R_T, the voltage of the microprobes was swept through a set range (-0.5-0.5 V) and the resultant current was measured. The R_T values were then plotted against the value of contact spacing *d* for each measurement. An example of such a TLM plot is shown in Figure 7-2. The slope

and the x-intercept of each plot was used to determine the sheet resistance R_{SH} and the transfer length L_T of each structure, respectively. The contact resistivity was then calculated using:

$$\rho_c = R_c L_T W \tag{7-1}$$

$R_c = contact\ resistance$

$W = contact\ dimension\ perpendicular\ to\ the\ current\ flow$

$L = contact\ dimension\ parallel\ to\ the\ current\ flow$

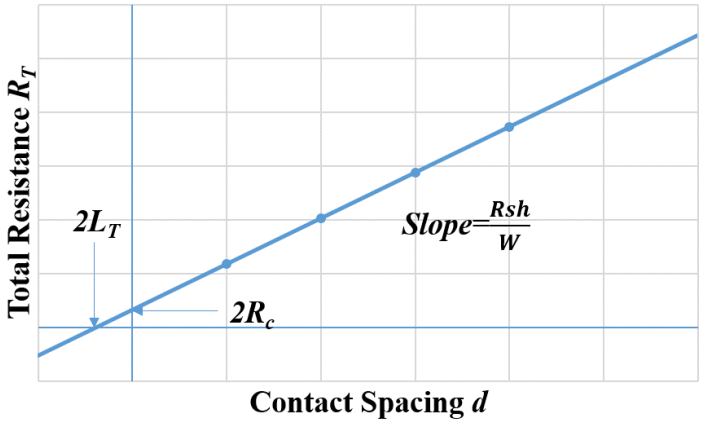

Figure 7-2: Fitted curve of total resistance versus contact spacing.

For both pre- and post-annealed samples, TEM specimens were prepared by focused ion beam (FIB) technique using a FIB FEI 200 TEM. Bright field (BF) and high resolution TEM (HRTEM) images of p-si/MoO_x/ITO stacks were obtained with the help of FEI TEM Tecnai F30 at an operating voltage of 300 KV. Electron energy loss

spectroscopy (EELS) studies were carried out in STEM mode with the help of JEOL ARM 200CF equipped with a cold field-emission gun and double-spherical aberration correctors at the Brookhaven National Laboratory operated at 200 kV. Multiple EELS line scans were carried out to detect any chemical change occurring after annealing.

7.3 Results and discussion

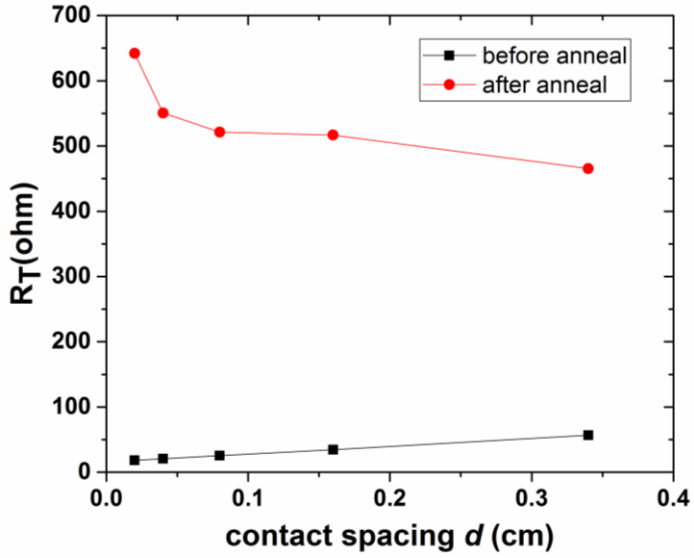

Figure 7-3: Total resistance (R_T) v/s contact spacing (d) plot to obtain contact resistivity of pre- and post-annealed samples from TLM

It can be seen from Figure 7-3 that although low contact resistivity value of 0.52 $\Omega.cm^2$ is obtained prior to annealing, it drastically increases upon annealing in air at 200°C for 30 min. This indicates that probably a hole-blocking interlayer is formed upon annealing which increases the contact resistivity. To investigate further, high-resolution TEM images were obtained for both pre-and post-annealed samples.

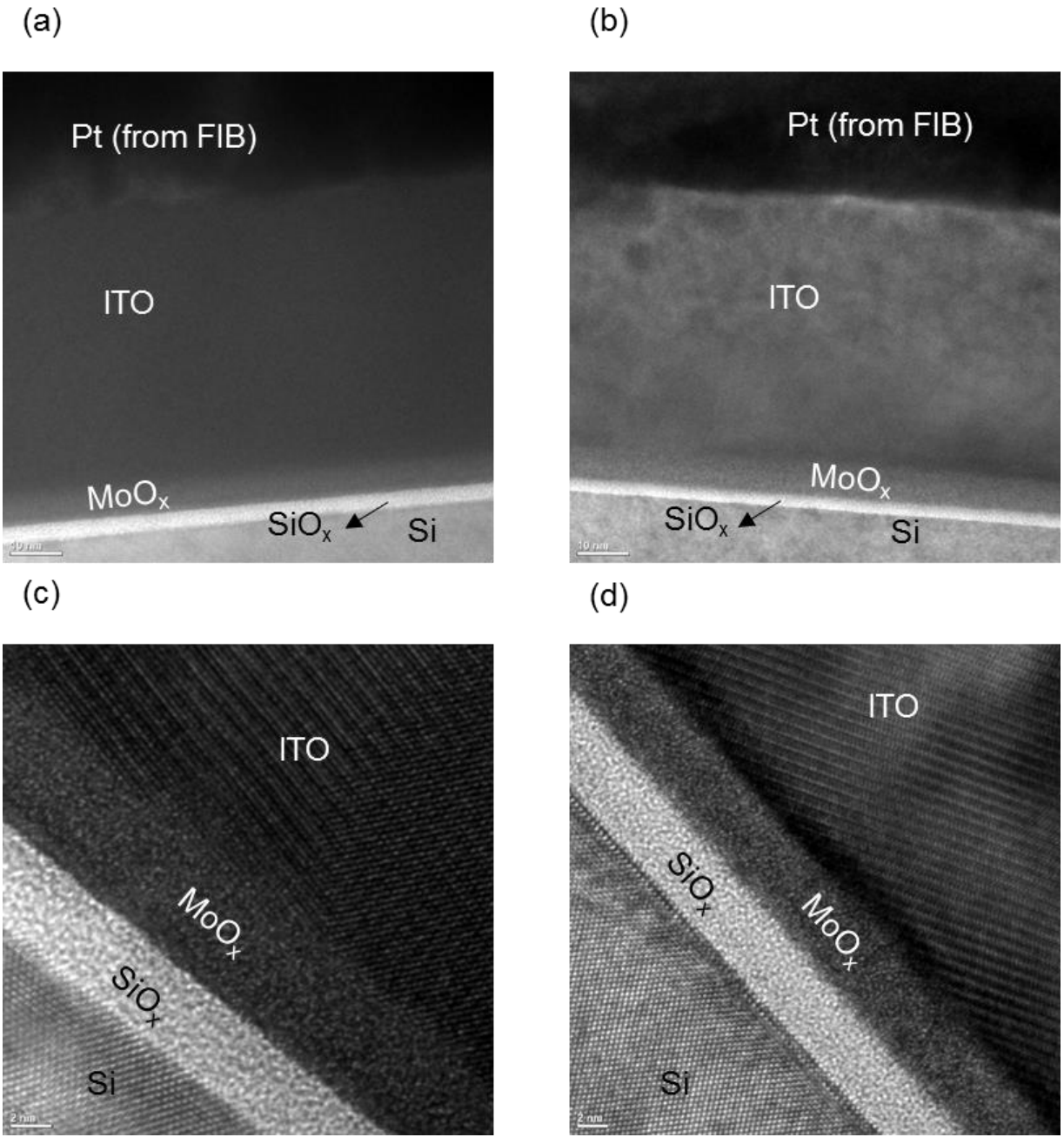

Figure 7-4: (a), (b) BF image of pre-and post-annealed samples respectively; (c), (d) HRTEM images of pre-and post-annealed samples respectively

It can be observed from Figure 7-4 that 2-3 nm SiO_x layer is formed at Si surface. Moreover, SiO_x layer is present in case of both pre- and post-annealed samples. This indicates that SiO_x layer was formed prior to anneal during the deposition process of MoO_x and ITO. However, no obvious interlayer is found at MoO_x/ITO interface even after annealing. Overall, HRTEM micrographs of pre- and post-anneal samples indicates no significant changes upon annealing. Therefore, to determine any chemical change occurring upon annealing which might be responsible for drastic increase in contact resistivity, multiple EELS line scan were carried out.

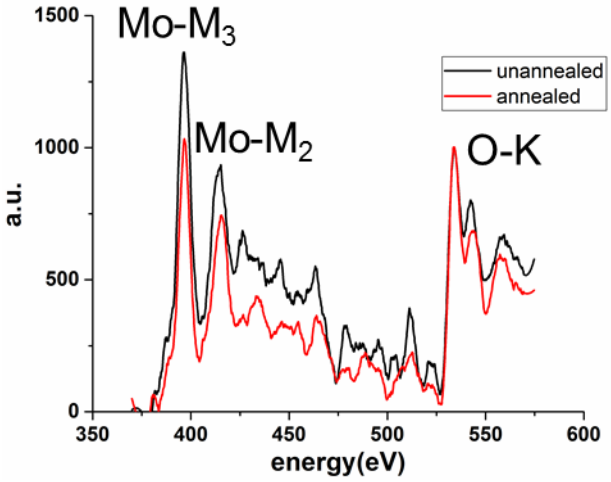

Figure 7-5: EELS line scan in bulk MoO_x for pre- and post-annealed samples

A typical EELS scan from bulk MoO_x for pre- and post-annealed samples is shown in Figure 7-5. It can be inferred from relative intensities of Mo-M_3 that stoichiometry of MoO_x phase changes upon annealing and it becomes less-oxygen deficient. Since annealing was done in air, oxygen diffuses into MoO_x phase and occupies vacant oxygen sites which reduces concentration of oxygen vacancies. Since, the semi-metallic

character of MoO_x is due to presence of oxygen vacancies, even a small reduction in oxygen vacancy concentration leads to sharp reduction in conductivity of MoO_x layer which in turn drastically increases contact resistivity as shown in Figure 7-3. Moreover, Geissbuhler et al. has previously reported that cell performance of MoO_x based cell degrades upon annealing at 130°C wherein FF drops from 76.6% to 69.7% and J-V curve becomes S-shaped. Therefore, it can be concluded that for cells featuring MoO_x contacts, annealing in air reduces conductivity of MoO_x layer which increases contact resistivity leading to drop in FF and lower cell performance.

7.4 Conclusion

In summary, when solar cells featuring a MoO_x/ITO based front contact upon annealing in air, oxygen diffusion into MoO_x which reduces concentration of oxygen vacancies in MoO_x and leads to drastic reduction in conductivity of MoO_x. Thus, overall contact resistivity increases which reduces FF resulting in a S-shaped J-V curve and deterioration of device performance.

CHAPTER 8:
CONCLUSION

Surface passivation plays an important role in obtaining very high efficiencies in c-Si solar cells. In this work, the impact of various surface preparation methods on passivation performance of SiN_x and Al_2O_3/SiN_x passivated {100} n-type Cz c-Si wafers was investigated in detail. Furthermore, transition metals oxides namely, TiO_2 and MoO_x were investigated as electron-selective and hole-selective contacts to be employed as front and rear contacts respectively for an n-type cell with a boron-emitter. The key findings of this study are listed below

- The various surface cleans were not found to have a significant impact on Al_2O_3/SiN_x passivation stacks.
- However, for SiN_x passivated Si, carrier lifetime was strongly influenced by cleaning variations and that an oxide-last cleaning step prior to deposition of SiN_x passivation layers was found to create a 1-2 nm SiO_x tunnel layer resulting in excellent carrier lifetimes.
- DIO_3+HF+HCl→HF→DIO_3 and HNO_3→HF→HNO_3 cleans emerged as potential low-cost alternatives to HCl+HF clean in the photovoltaics industry.
- It was revealed that a low efficiency of 9.8% was obtained for cells featuring a-Si:H/TiO_2 rear contact which can be attributed to rapid degradation of surface passivation of a-Si:H upon FGA at 350°C due to hydrogen evolution leading to generation of defect states which increases recombination and hence a much lower V_{oc} of 365 mV is obtained.

- On the other hand, 21.6% efficiency for cells featuring SiO_2/TiO_2 rear contact is due to excellent passivation of SiO_2/TiO_2 stack upon FGA anneal which can be attributed to the presence of 1-2 nm SiO_2 layer whose passivation performance improves upon FGA at 350°C whereas presence of large number of oxygen vacancies in TiO_{2-x} reduces rear contact resistivity.
- It was revealed that degradation of device performance of an n-type cell featuring MoO_x/ITO front contact is due to oxygen diffusion into MoO_x upon annealing in air which reduces concentration of oxygen vacancies in MoO_x which drastically reduces MoO_x conductivity due to which overall contact resistivity increases. The increase in contact resistivity reduces FF and deterioration of device performance.

REFERENCES

[1] T.M. Razykov, C.S. Ferekides, D. Morel, E. Stefanakos, H.S. Ullal, H.M. Upadhyaya, Solar photovoltaic electricity: Current status and future prospects, Solar Energy 85(8) (2011) 1580-1608.

[2] A. Goetzberger, J. Luther, G. Willeke, Solar cells: past, present, future, Solar Energy Materials and Solar Cells 74 (2002) 1-11.

[3] A. Shah, P. Torres, R. Tscharner, N. Wyrsch, H. Keppner, Photovoltaic Technology: The Case for Thin-Film Solar Cells, Science 285(5428) (1999) 692-698.

[4] Handbook of Photovoltaic Science and Engineering, 2003.

[5] R.W. Miles, K.M. Hynes, I. Forbes, Photovoltaic solar cells: An overview of state-of-the-art cell development and environmental issues, Progress in Crystal Growth and Characterization of Materials 51(1-3) (2005) 1-42.

[6] A. Goetzberger, C. Hebling, H.-W. Schock, Photovoltaic materials, history, status and outlook, Materials Science and Engineering: R: Reports 40(1) (2003) 1-46.

[7] K.L. Chopra, P.D. Paulson, V. Dutta, Thin-film solar cells: an overview, Progress in Photovoltaics: Research and Applications 12(2-3) (2004) 69-92.

[8] Department of Economic United Nations and Population Division Social Affairs. World Population Prospects: The 2015 Revision., 2015.

[9] R.K. Pachauri Core Writing Team and L.A. Meyer (eds.). IPCC, 2014: Climate Change 2014: Synthesis Report. Contribution of Working Groups I, II and III to the Fifth Assessment Report of the Intergovernmental Panel on Climate Change. Technical report, IPCC, Geneva, Switzerland, 2014.

[10] http://hyperphysics.phy-astr.gsu.edu/hbase/Solids/pnjun.html#c3.).

[11]https://stuff.mit.edu/afs/athena.mit.edu/course/3/3.082/www/team2_f02/Pages/background.html.).

[12] https://pvpmc.sandia.gov/wp-content/uploads/2012/04/Single-Diode-EC2.png.).

[13] G.A. Armin, B.B. Matthew, H. Bram, M. Thomas, Industrial Silicon Wafer Solar Cells – Status and Trends, GREEN, 2012, p. 135.

[14] G. Dingemans, W.M.M. Kessels, Status and prospects of Al_2O_3-based surface passivation schemes for silicon solar cells, Journal of Vacuum Science & Technology A 30(4) (2012) 040802.

[15] M.A. Green, K. Emery, Y. Hishikawa, W. Warta, E.D. Dunlop, D.H. Levi, A.W.Y. Ho-Baillie, Solar cell efficiency tables (version 49), Progress in Photovoltaics: Research and Applications 25(1) (2017) 3-13.

[16] A.G. Aberle, Surface Passivation of Crystalline Silicon Solar Cells: A Review, Progress in Photovoltaics: Research and Applications 8 (2000) 473-487.

[17] K. Ding, M. Pomaska, A. Singh, F. Lentz, F. Finger, U. Rau, Mechanism for crystalline Si surface passivation by the combination of SiO_2 tunnel oxide and µc-SiC:H thin film, physica status solidi (RRL) – Rapid Research Letters 9999(9999) (2015) n/a-n/a.

[18] S.W. Glunz, D. Biro, S. Rein, W. Warta, Field-effect passivation of the SiO_2/Si interface, Journal of Applied Physics 86(1) (1999) 683-691.

[19] A.G. Aberle, Overview on SiN surface passivation of crystalline silicon solar cells, Solar Energy Materials and Solar Cells 65(1–4) (2001) 239-248.

[20] D.D. Cohen, R. Siegele, T. Chandra, M. Ionescu, B. Richards, K. McIntosh, E. Stelcer, Hydrogen Measurements in SiN_x:H/Si thin films by ERDA, Materials science forum 539 (2007) 3551-3556.

[21] J. Bullock, D. Yan, Y. Wan, A. Cuevas, B. Demaurex, A. Hessler-Wyser, S. De Wolf, Amorphous silicon passivated contacts for diffused junction silicon solar cells, Journal of Applied Physics 115(16) (2014) 163703.

[22] B.n.d. Demaurex, S. De Wolf, A. Descoeudres, Z. Charles Holman, C. Ballif, Damage at hydrogenated amorphous/crystalline silicon interfaces by indium tin oxide overlayer sputtering, Applied Physics Letters 101(17) (2012) 171604.

[23] J. Benick, B. Hoex, M.C.M. van de Sanden, W.M.M. Kessels, O. Schultz, S.W. Glunz, High efficiency n-type Si solar cells on Al_2O_3-passivated boron emitters, Applied Physics Letters 92(25) (2008) 253504.

[24] G. Dingemans, W. Beyer, M.C.M. van de Sanden, W.M.M. Kessels, Hydrogen induced passivation of Si interfaces by Al_2O_3 films and SiO_2/Al_2O_3 stacks, Applied Physics Letters 97(15) (2010) 152106.

[25] G. Dingemans, N.M. Terlinden, M.A. Verheijen, M.C.M. van de Sanden, W.M.M. Kessels, Controlling the fixed charge and passivation properties of $Si(100)/Al_2O_3$ interfaces using ultrathin SiO_2 interlayers synthesized by atomic layer deposition, Journal of Applied Physics 110(9) (2011) 093715.

[26] B. Hoex, S.B.S. Heil, E. Langereis, M.C.M. van de Sanden, W.M.M. Kessels, Ultralow surface recombination of c-Si substrates passivated by plasma-assisted atomic layer deposited Al_2O_3, Applied Physics Letters 89(4) (2006) 042112-1-042112-3.

[27] F.-C. Chiu, Surface State Capture Cross-Section at the Interface between Silicon and Hafnium Oxide, Advances in Materials Science and Engineering 2013 (2013) 1-5.

[28] J. Wang, S.S. Mottaghian, M.F. Baroughi, Passivation Properties of Atomic-Layer-Deposited Hafnium and Aluminum Oxides on Si Surfaces, Electron Devices, IEEE Transactions on 59(2) (2012) 342-348.

[29] X. Yang, Q. Bi, H. Ali, K. Davis, W.V. Schoenfeld, K. Weber, High-Performance TiO2-Based Electron-Selective Contacts for Crystalline Silicon Solar Cells, Advanced Materials 28(28) (2016) 5891-5897.

[30] C. Battaglia, X. Yin, M. Zheng, I.D. Sharp, T. Chen, S. McDonnell, A. Azcatl, C. Carraro, B. Ma, R. Maboudian, R.M. Wallace, A. Javey, Hole selective MoO_x contact for silicon solar cells, Nano letters 14(2) (2014) 967-71.

[31] M. Bivour, J. Temmler, H. Steinkemper, M. Hermle, Molybdenum and tungsten oxide: High work function wide band gap contact materials for hole selective contacts of silicon solar cells, Solar Energy Materials and Solar Cells 142 (2015) 34-41.

[32] J. Bullock, A. Cuevas, T. Allen, C. Battaglia, Molybdenum oxide MoO_X: A versatile hole contact for silicon solar cells, Applied Physics Letters 105(23) (2014) 232109.

[33] L.G. Gerling, S. Mahato, A. Morales-Vilches, G. Masmitja, P. Ortega, C. Voz, R. Alcubilla, J. Puigdollers, Transition metal oxides as hole-selective contacts in silicon heterojunctions solar cells, Solar Energy Materials and Solar Cells 145 (2016) 109-115.

[34] D.P. Sánchez, Crystalline silicon heterojunction solar cells, Universitat Politècnica de Catalunya, 2015.

[35] S. Avasthi, W.E. McClain, G. Man, A. Kahn, J. Schwartz, J.C. Sturm, Hole-blocking titanium-oxide/silicon heterojunction and its application to photovoltaics, Applied Physics Letters 102(20) (2013) 203901.

[36] L.E. Black, K.R. McIntosh, Surface passivation of c-Si by atmospheric pressure chemical vapor deposition of Al_2O_3, Applied Physics Letters 100(20) (2012) 202107-1-202107-5.

[37] K.O. Davis, K. Jiang, M. Wilson, C. Demberger, H. Zunft, H. Haverkamp, D. Habermann, W.V. Schoenfeld, Influence of precursor gas ratio and firing on silicon surface passivation by APCVD aluminium oxide, physica status solidi (RRL) – Rapid Research Letters 7(11) (2013) 942-945.

[38] I. Dirnstorfer, D.K. Simon, P.M. Jordan, T. Mikolajick, Near surface inversion layer recombination in Al_2O_3 passivated n-type silicon, Journal of Applied Physics 116(4) (2014) 044112.

[39] M.J. Kerr, J. Schmidt, A. Cuevas, J.H. Bultman, Surface recombination velocity of phosphorus-diffused silicon solar cell emitters passivated with plasma enhanced chemical vapor deposited silicon nitride and thermal silicon oxide, Journal of Applied Physics 89(7) (2001) 3821.

[40] M. Bivour, C. Reichel, M. Hermle, S.W. Glunz, Improving the a-Si:H(p) rear emitter contact of n-type silicon solar cells, Solar Energy Materials and Solar Cells 106 (2012) 11-16.

[41] J. Bullock, A. Cuevas, C. Samundsett, D. Yan, J. McKeon, Y. Wan, Simple silicon solar cells featuring an a-Si:H enhanced rear MIS contact, Solar Energy Materials and Solar Cells 138 (2015) 22-25.

[42] D.Y. Kim, E. Guijt, R.A.C.M.M. van Swaaij, M. Zeman, Development of a-SiO_x:H solar cells with very high $V_{oc} \times FF$ product, Progress in Photovoltaics: Research and Applications 23(6) (2015) 671-684.

[43] S. Duttagupta, F. Lin, K.D. Shetty, A.G. Aberle, B. Hoex, Excellent boron emitter passivation for high-efficiency Si wafer solar cells using AlO_x/SiN_x dielectric stacks deposited in an industrial inline plasma reactor, Progress in Photovoltaics: Research and Applications 21(4) (2013) 760-764.

[44] D. Garcia-Alonso, S. Smit, S. Bordihn, W.M.M. Kessels, Silicon passivation and tunneling contact formation by atomic layer deposited Al_2O_3/ZnO stacks, Semiconductor Science and Technology 28(8) (2013) 082002.

[45] K.S. Jeong, H.M. Kwon, H.D. Lee, G.W. Lee, Ultra-thin aluminum oxide as an interface passivation layer for ZnO/p-Si heterojunction solar cells, physica status solidi (a) (2014) n/a-n/a.

[46] S. Duttagupta, Z. Hameiri, T. Grosse, D. Landgraf, B. Hoex, A.G. Aberle, Dielectric Charge Tailoring in PECVD SiO_x/SiN_x Stacks and Application at the Rear of Al Local Back Surface Field Si Wafer Solar Cells, IEEE Journal of Photovoltaics 5(4) (2015) 1014-1019.

[47] A. Laades, H.-P. Sperlich, M. Bähr, U. Stürzebecher, C.A. Diaz Alvarez, M. Burkhardt, H. Angermann, M. Blech, A. Lawerenz, On the impact of interfacial SiO_x-layer

on the passivation properties of PECVD synthesized aluminum oxide, physica status solidi (c) 9(10-11) (2012) 2120-2123.

[48] J.A. Töfflinger, A. Laades, L. Korte, C. Leendertz, L.M. Montañez, U. Stürzebecher, H.-P. Sperlich, B. Rech, PECVD-AlO_x/SiN_x passivation stacks on wet chemically oxidized silicon: Constant voltage stress investigations of charge dynamics and interface defect states, Solar Energy Materials and Solar Cells 135 (2015) 49-56.

[49] Y. Wan, J. Bullock, A. Cuevas, Passivation of c-Si surfaces by ALD tantalum oxide capped with PECVD silicon nitride, Solar Energy Materials and Solar Cells 142 (2015) 42-46.

[50] S. Dauwe, L. Mittelstädt, A. Metz, R. Hezel, Experimental evidence of parasitic shunting in silicon nitride rear surface passivated solar cells, Progress in Photovoltaics: Research and Applications 10(4) (2002) 271-278.

[51] B. Hoex, J. Schmidt, P. Pohl, M.C.M. van de Sanden, W.M.M. Kessels, Silicon surface passivation by atomic layer deposited Al_2O_3, Journal of Applied Physics 104(4) (2008) 044903.

[52] International Technology Roadmap for Photovoltaics, SEMI, 2015.

[53] A. Moldovan, K. Birmann, J. Rentsch, M. Zimmer, T. Gitte, J. Fittkau, Combined Ozone/HF/HCI based cleaning and adjusted emitter etch-back for silicon solar cells, Solid State Phenomena 195 (2013) 305-309.

[54] I. Kuzma-Filipek, M. Recaman-Payo, M. Aleman, J. John, M. Haslinger, E. Cornagliotti, F. Duerinckx, A. Hajjiah, M. Soha, R. Russel, A. Sharma, A. Uruena, J.

Szlufcik, I. Gordon, Simplified cleaning for 22.5% nPERT solar cells with rear epitaxial emitters, Solar Energy Materials and Solar Cells 158 (2016) 19-23.

[55] K.O. Davis, I. Kashkoush, A. Blum, K. Ogutman, E. Schneller, R.A. Sinton, W.V. Schoenfeld, Impact of ozone-based cleaning on surface recombination with different passivation materials, Photovoltaic Specialist Conference (PVSC), 2015 IEEE 42nd, 2015, pp. 1-3.

[56] Y.-C. Hu, M.-H. Chiu, L. Wang, J.-L. Tsai, Efficiency Improvement of Silicon Solar Cells by Nitric Acid Oxidization, Japanese Journal of Applied Physics 49(2) (2010) 022301.

[57] C. Kranz, S. Wyczanowski, U. Baumann, S. Dorn, S. Queisser, J. Schweckendiek, D. Pysch, T. Dullweber, Industrial Cleaning Sequences for Al_2O_3-passivated PERC Solar Cells, Energy Procedia 55 (2014) 211-218.

[58] T. Matsumoto, R. Hirose, F. Shibata, D. Ishibashi, S. Ogawara, H. Kobayashi, Nitric acid oxidation of Si method for improvement of crystalline Si solar cell characteristics by surface passivation effect, Solar Energy Materials and Solar Cells 134 (2015) 298-304.

[59] V.D. Mihailetchi, Y. Komatsu, L.J. Geerligs, Nitric acid pretreatment for the passivation of boron emitters for n-type base silicon solar cells, Applied Physics Letters 92(6) (2008) 63510-63510.

[60] A. Moldovan, F. Feldmann, M. Zimmer, J. Rentsch, J. Benick, M. Hermle, Tunnel oxide passivated carrier-selective contacts based on ultra-thin SiO_2 layers, Solar Energy Materials and Solar Cells 142 (2015) 123-127.

[61] D.E. Kane, R.M. Swanson, Measurement of the emitter saturation current by a contactless photoconductivity decay method, 18th IEEE Photovoltaic Specialists Conference, Las Vegas, NV, USA, 1985, pp. 578-583.

[62] M. Wilson, D. Marinskiy, A. Byelyayev, J. D'Amico, A. Findlay, L. Jastrzebski, J. Lagowski, The Present Status and Recent Advancements in Corona-Kelvin Non-Contact Electrical Metrology of Dielectrics for IC-Manufacturing, ECS Transactions 3 (2006) 3-24.

[63] M. Spitz, U. Belledin, S. Rein, Fast Inductive Inline Measurement of the Emitter Sheet Resistance in Industrial Solar Cell Fabrication, 22nd European Photovoltaic Solar Energy Conference and Exhibition, Milan, Italy, 2007.

[64] P.P. Altermatt, H. Plagwitz, R. Bock, J. Schmidt, R. Brendel, M.J. Kerr, A. Cuevas, The surface recombination velocity at boron-doped emitters: comparison between various passivation techniques, 21st European Photovoltaic Solar Energy Conference and Exhibition, Dresden, Germany, 2006, pp. 647-650.

[65] P.P. Altermatt, Models for numerical device simulations of crystalline silicon solar cells—a review, Journal of Computational Electronics 10(3) (2011) 314.

[66] F. Werner, B. Veith, D. Zielke, L. Kühnemund, C. Tegenkamp, M. Seibt, R. Brendel, J. Schmidt, Electronic and chemical properties of the c-Si/Al_2O_3 interface, Journal of Applied Physics 109(11) (2011) 113701.

[67] W. Zhang, K.O. Davis, W.V. Schoenfeld, P. Looney, F. Wang, STEM-EELS Studies of the Local Structure and Coordination of Al_2O_3/Si interfaces in Si Solar Cells, Microscopy and Microanalysis 20(S3) (2014) 396-397.

[68] C. Battaglia, S.M. de Nicolás, S. De Wolf, X. Yin, M. Zheng, C. Ballif, A. Javey, Silicon heterojunction solar cell with passivated hole selective MoO_x contact, Applied Physics Letters 104(11) (2014) 113902.

[69] F. Feldmann, M. Simon, M. Bivour, C. Reichel, M. Hermle, S.W. Glunz, Carrier-selective contacts for Si solar cells, Applied Physics Letters 104(18) (2014) 181105.

[70] J. Peter Seif, A. Descoeudres, M. Filipič, F. Smole, M. Topič, Z. Charles Holman, S. De Wolf, C. Ballif, Amorphous silicon oxide window layers for high-efficiency silicon heterojunction solar cells, Journal of Applied Physics 115(2) (2014) 024502.

[71] S. De Wolf, A. Descoeudres, Z.C. Holman, C. Ballif, High-efficiency Silicon Heterojunction Solar Cells: A Review, green 2(1) (2012).

[72] X. Yang, K. Weber, N-type silicon solar cells featuring an electron-selective TiO_2 contact, Photovoltaic Specialist Conference (PVSC), 2015 IEEE 42nd, 2015, pp. 1-4.

[73] K.A. Nagamatsu, Crystalline Silicon Photovoltaics via Low-Temperature TiO_2/Si and PEDOT/Si Heterojunctions, Princeton University, 2015.

[74] X. Yang, P. Zheng, Q. Bi, K. Weber, Silicon heterojunction solar cells with electron selective TiO_x contact, Solar Energy Materials and Solar Cells 150 (2016) 32-38.

[75] X. Cheng, E.S. Marstein, H. Haug, C.C. You, M. Di Sabatino, Thermal stability of hydrogenated amorphous silicon passivation for p-type crystalline silicon, physica status solidi (a) 213(1) (2016) 91-95.

[76] D. Zhang, A. Tavakoliyaraki, Y. Wu, R.A.C.M.M. van Swaaij, M. Zeman, Influence of ITO deposition and post annealing on HIT solar cell structures, Energy Procedia 8 (2011) 207-213.

[77] J. Bullock, M. Hettick, J. Geissbühler, A.J. Ong, T. Allen, Carolin M. Sutter-Fella, T. Chen, H. Ota, E.W. Schaler, S. De Wolf, C. Ballif, A. Cuevas, A. Javey, Efficient silicon solar cells with dopant-free asymmetric heterocontacts, Nature Energy (2016) 15031.

[78] J. Geissbühler, J. Werner, S.M.d. Nicolas, L. Barraud, A. Hessler-Wyser, M. Despeisse, S. Nicolay, A. Tomasi, B. Niesen, S.D. Wolf, C. Ballif, 22.5% efficient silicon heterojunction solar cell with molybdenum oxide hole collector, Applied Physics Letters 107(8) (2015) 081601.